Distribution Agreement

In presenting this thesis or dissertation as a partial fulfillment of the requirements for an advanced degree from Emory University, I hereby grant to Emory University and its agents the non-exclusive license to archive, make accessible, and display my thesis or dissertation in whole or in part in all forms of media, now or hereafter known, including display on the world wide web. I understand that I may select some access restrictions as part of the online submission of this thesis or dissertation. I retain all ownership rights to the copyright of the thesis or dissertation. I also retain the right to use in future works (such as articles or books) all or part of this thesis or dissertation.

Signature:

_____ _____

Thomas Austin Nuckols Date

Comparison of two models of *GRN*-deficiency using quantitative proteomics

By

T. Austin Nuckols

Thomas Kukar, Ph.D.
Advisor

Chadwick Hales, M.D., Ph.D.
Advisor

T.J. Murphy, Ph.D.
Committee Member

John Hepler, Ph.D.
Committee Member

Accepted:

Kimberly Jacob Arriola, Ph.D, MPH
Dean of the James T. Laney School of Graduate Studies

Date

Comparison of two models of *GRN*-deficiency using quantitative proteomics

By

T. Austin Nuckols
B.S., University of Georgia, 2016

Advisors:
Chadwick Hales, M.D., Ph.D.
Thomas Kukar, Ph.D.

An abstract of
a thesis submitted to the Faculty of the
James T. Laney School of Graduate Studies of Emory University
in partial fulfillment of the requirements for the degree of
Master of Science
in Molecular and Systems Pharmacology
2022

Abstract

Comparison of two models of *GRN*-deficiency using quantitative proteomics

By T. Austin Nuckols

Mutations in the gene *Granulin* (*GRN*) reduce levels of progranulin (PGRN) and result in the neurodegenerative diseases frontotemporal dementia (FTD) and neuronal ceroid lipofuscinosis. PGRN has been implicated in high level functions like neurite outgrowth, neuronal survival, and inflammation while its molecular function is hypothesized to occur in the lysosome. Accordingly, *GRN* is highly expressed in neurons and microglia. *GRN*-deficiency is marked by increased inflammation, lysosome dysfunction, and recently, dysfunction in lipid metabolism and catabolism. Various models are used to study these different features of *GRN*-deficiency. Here, I compare proteomic datasets from *Grn* WT and KO mouse embryonic fibroblasts (MEFs) and *GRN* WT and KO induced pluripotent stem cell-derived microglia (iPSC-microglia). Despite little overlap of proteins significant in both cell types, several pathways are significantly overrepresented in multiple genotype/cell model combinations like pathways containing “organelle” and “cellular response to stress.” Additionally, each subset identifies unique features of *GRN*-pathology, and each cell type offers protein targets to pursue. Overall, these analyses support the hypothesis that *GRN* pathology is driven by dysfunction in lysosomal lipid metabolism and catabolism resulting in the accumulation of lipids. Altogether, these analyses identify unique features of *GRN*-deficiency and support the use of MEFs as a model to study lipid accumulation in FTD and iPSC-microglia as a model for studying inflammation and possibly lipid droplet formation in FTD.

Comparison of two models of *GRN*-deficiency using quantitative proteomics

By

T. Austin Nuckols
B.S., University of Georgia, 2016

Advisors:
Chadwick Hales, M.D., Ph.D.
Thomas Kukar, Ph.D.

A thesis submitted to the Faculty of the
James T. Laney School of Graduate Studies of Emory University
in partial fulfillment of the requirements for the degree of
Master of Science
in Molecular and Systems Pharmacology
2022

Contents

Figures

Tables

Supplemental Figures

Supplemental Tables

Introduction

Frontotemporal dementia (FTD) is a leading cause of dementia in people under the age of 60 with a median survival 8-9 years after diagnosis [1] and no existing cure. Heterozygous mutations in the granulin gene (*GRN*) are responsible for 25% of familial FTD cases [2-4]. FTD due to *GRN* mutations is characterized by intraneuronal protein inclusions positive for ubiquitin and transactive response DNA-binding protein 43 (TDP-43), a diagnostic hallmark of FTD [5, 6]. Homozygous *GRN* mutations cause neuronal ceroid lipofuscinosis (NCL) subtype 11 [7, 8], a neurodegenerative lysosomal storage disease. NCL is characterized by the lysosomal accumulation of lipofuscin, an autofluorescent and undegraded accumulation of proteins, lipids, and metals [9]. *GRN* mutations result in decreased levels of progranulin (PGRN) with heterozygous mutations producing a 50-75% decrease in PGRN while homozygous mutations result in complete ablation of PGRN [10-12]. FTD and NCL due to *GRN*-mutations share several pathological features suggesting common underlying mechanisms that lead to different clinical presentations based on the degree of *GRN*-deficiency [7].

PGRN is a secreted glycoprotein that consists of 7.5 individual 6 kDa granulin domains [13-15]. In the brain, PGRN is most heavily expressed in neurons and microglia [16] and is implicated in neuronal survival, neurite outgrowth, and inflammation [17-19]. PGRN is trafficked to the lysosome via the sortilin receptor [20-22] or via co-trafficking with prosaposin (PSAP) [23]. PGRN has been purported to bind to lysosomal proteins cathepsin D (CTSD) [24-27], β-hexosaminidase-A (HexA) [28], and β-glucocerebrosidase (GBA) [29, 30], but its molecular function remains unknown.

Various models have been used to study FTD-*GRN* including five unique *Grn*$^{-/-}$ mouse models, several immortalized cell lines, and patient tissue and patient-derived cell lines [31]. Overall, *GRN*-deficiency is neuropathologically marked by astrogliosis, microgliosis, neuronal cell death [32], as well as the accumulation of lipofuscin, TDP-43, p62, and ubiquitin [32-36]. Models of *GRN*-deficiency also demonstrate marked lysosome dysfunction including altered lysosomal enzyme activity and changes to

lysosome protein expression [24, 27-30, 36-41], and more recently, changes to lipid metabolism and catabolism [42-45].

Different FTD-*GRN* models allow researchers to study different features of *GRN*-related pathology. In this work, I compare two models of *GRN*-deficiency using quantitative proteomic analysis. We submitted 3 replicates of *Grn* wild-type (WT) and *Grn* knockout (KO) mouse embryonic fibroblasts (MEFs) to label-free quantification liquid chromatography tandem mass spectrometry (LFQ LC-MS/MS) to identify novel protein and biological pathway targets. Separately, collaborators independently submitted 5 and 4 replicates, respectively, of *GRN* WT and KO induced pluripotent stem cell-derived microglia (iPSC-microglia) lines to LFQ LC-MS/MS. Here, I analyze and compare both datasets using differential expression analysis and pathway overrepresentation analysis.

Results

Data Imputation

LFQ intensity values were obtained from raw counts using the MaxLFQ algorithm. Given the apparent homogeneity of variances within subsets and similar medians (**Figures 1-4**), neither normalization nor variance-stabilizing transformations were pursued. 4.96% of values in the MEF data were missing found in 525 of 3990 proteins total (**Figure 5**). The MEF WT subset had 3.14% of values missing while the MEF KO subset had 2.41% of values missing. 121 proteins were completely missing in the MEF WT subset, and 53 proteins were completely missing in MEF KO subset. 11.84% of values in the iPSC-microglia data were missing. These missing values were found across 1072 of 3316 proteins total (**Figure 5**). The iPSC-microglia WT subset had 8.52% of values missing while the iPSC-microglia KO subset had 10.01% of values missing. 22 proteins were completely missing in the iPSC-microglia WT subset while 171 proteins were completely missing in the iPSC-microglia KO subset.

Each subset of data (i.e., MEF WT, MEF KO, iPSC WT, iPSC KO) was imputed using a random forest algorithm implemented in the MissForest R package [46]. The random forest algorithm was found to be the highest performing method in a comparative study of the effect of multiple imputation methods on label-free proteomics data including at dataset from immune cells [47]. Regardless, the accuracy of the MissForest imputation algorithm was empirically tested on these data by artificially introducing missing values into each subset of data, imputing those values, and measuring the imputed values against the known values. The error metric used was normalized root mean square error (NRMSE) as measured by Oba et al. 2003. The following protocol was used. Proteins with actual missing values were filtered out of each subset producing the "filtered subset." Then, randomly selected values were removed and left empty to induce missingness in each filtered subset. The number of values removed from each filtered subset was set to be identical to the actual proportion of missing values in the original subset (*e.g.*, the MEF WT filtered subset had 3.14% of values removed to induce missingness). Those missing values were imputed back with the random forest algorithm. The estimated NRMSE supplied by the algorithm was collected, and the true NRMSE was calculated by comparing the imputed values to the original values. This protocol was performed twenty times for each subset across two "number of trees" hyperparameter settings (100 or 500 trees) which combined to produce forty total simulations per subset. Twenty simulations per subset per number of trees setting was chosen due to high computation times.

Overall, the algorithm performed well with all median true error rates being less than 0.18 (**Supplemental Figure 1A**). For reference, NRMSE values approaching 0 represent near perfect fits between estimated and true values while NRMSE values approaching 1.0 represent estimations being equivalent to a random guess [48]. Comparatively, the algorithm performed equally well on the MEF WT and MEF KO subsets while the iPSC-microglia KO subset had a much higher true error rate than the iPSC-microglia WT subset despite having only a 1.49% difference in number of values missing. There was no effect of the number of trees on error rate. The estimated error rate, which is supplied by the

MissForest() function, was strongly correlated with the true error rate (**Supplemental Figure 1B**) suggesting it can be used to infer the performance of the algorithm on the actual missing data.

The random forest algorithm was used to impute the actual missing values in each subset. The "number of trees" hyperparameter setting was set to 100. Interestingly, estimated NRMSE values were much lower for the actual imputations compared to those of the simulations. The estimated NRMSE values for each subset were the following: 0.072 for MEF WT, 0.095 for MEF KO, 0.100 for iPSC-microglia WT, and 0.064 for iPSC-microglia KO. Together, the strong correlation between the true NRMSE and estimated NRMSE rates in the simulation results (**Supplemental Figure 1B**) and the low estimated NRMSE rates during the actual imputation suggest that the random forest algorithm performed very well during the actual imputation.

Differential Expression Analysis

Differential expression analysis was performed between WT and KO MEFS and between WT and KO iPSC-microglia using Student's T-tests with Benjamini-Hochberg False Discovery Rate (FDR) to correct for multiple comparisons. The proteomic analysis of the iPSC-microglia is tied to our collaborator's RNA sequencing analysis using the same cell lines. Their analysis considered proteins significantly differentially expressed when they had an absolute $\log_2$ fold-change > 1 and an adjusted q-value < 0.05. Therefore, the same criteria were used for both the WT and KO MEFs and the WT and KO iPSC-microglia. This resulted in 614 significant proteins in the MEFs (15.39% of proteins) and 264 significant proteins in the iPSC-microglia (7.96% of proteins) (**Figures 6-9**). To note, proteins found exclusively in the WT or KO subset for each cell-type are included in the groups of significant proteins.

To compare protein expression values for individual proteins found in both the MEF and iPSC-microglia datasets, protein homologs were identified and converted to matching names using the *gorth()* function in gProfiler2. There were 2245 homologous proteins shared between the cell types out of the original 3990 in the MEFs and 3316 in the iPSC-microglia. Overall, there was no pairwise correlation of

log_2 fold-change values between homologs; however, several proteins are found in only the WT or KO subset of one cell type while being found in both subsets of the other cell type (*data not shown*).

Despite the relatively large overlap of proteins present in both datasets, only 23 proteins were significant in both differential expression analyses (**Table 1**). Moreover, of these 23 proteins, only translocator protein (TSPO) and metallothionein-1 (MT1) returned results from a PubMed fetch using queries Q_GRN1 and Q_FTD1 (*See Methods: PubMed Fetching*). TSPO is a biomarker for microglia activation [49] and is the target of several positron emission tomography (PET) ligands used to identify Alzheimer's Disease, FTD, Parkinson's Disease and other neuroinflammatory disorders [50]. TSPO is overexpressed in MEF KO although, interestingly, it is also overexpressed in iPSC-microglia WT. TSPO's overexpression in iPSC-microglia WT conflicts with a report showing increased TSPO PET signal in both an FTD patient and *Grn*$^{-/-}$ mouse brain [51] as well as with literature which supports the idea that *GRN*-deficiency results in increased microglial activation [37, 38, 52-54]. MT1 is a metal-binding protein that functions to detoxify heavy metals, maintain zinc and copper homeostasis, and scavenge free radicals [55]. Here, MT1 is overexpressed in both MEF KO and iPSC-microglia KO which supports another group's findings of increased immunostaining for MT1 and MT2 in the brains of FTD patients [56]. To note, metallothionein-2 (MT2) is also overexpressed in MEF KO with a log_2 fold-change of 3.16 ($q = 0.00164$).

Pathway Overrepresentation Analysis

Significant proteins in each subset were used to perform overrepresentation analysis (ORA) with the gProfiler2 R package [57]. ORA was performed testing for significant pathways in the Gene Ontology (GO) [58, 59], Kyoto Encyclopedia of Genes and Genomes (KEGG) [60], Reactome (REAC) [61], and WikiPathways (WP) [62] databases. GO pathways with nominal p-values < 0.05 were pruned using REVIGO [63] which utilized the *simRel* formula to determine semantic similarity between GO terms [64]. The similarity coefficient threshold was set to 0.5 (considered allowing only "small" overlap). After

pruning, the ORA p-values were corrected for multiple comparisons using the Holm method for the MEFs and FDR for the iPSC-microglia. Pathways with p-values < 0.01 (MEFs) or q-values < 0.01 (iPSC-microglia) were considered significant. While the FDR method is commonly used to adjust p-values following ORA [65], here the Holm method was chosen *post hoc* after seeing an extremely high number of significant pathways overrepresented in MEF WT and in MEF KO using FDR (*data not shown*).

There were 169 significant pathways in the MEF WT subset, 84 in the MEF KO subset, 112 in the iPSC-microglia WT subset, and 38 in the iPSC-microglia KO subset. Despite pruning the GO pathways, there was still a large level of redundancy within the GO terms. For several figures and tables, GO terms that exist at level two of their hierarchies were removed to reduce this redundancy and highlight more specific significant pathways as well as pathways from other source databases. Pathways from the other databases were not filtered out using the level two criterium. Importantly, this does not impact the p-value adjustment which was performed prior to this step, and the full lists of significant pathways are available in the supplement.

Several significant pathways were shared between the different subsets (**Table 2 and Supplemental Table 1**). Unsurprisingly, the pathways "Intracellular membrane-bounded organelle," "intracellular organelle," "organelle membrane," and "vacuole" were shared between at least two of the subsets, partially represented by the known association between lysosome dysfunction and FTD and autophagic dysfunction and FTD [66]. To note, "lysosome" and "vesicle" were also significant terms in both iPSC-microglia WT and iPSC-microglia KO (**Supplemental Table 1**). Several proteins that constitute these pathways have reported connections to FTD or *GRN*-deficiency in the literature. **Table 3** lists proteins that constituted at least one of the significant pathways "intracellular membrane-bounded organelle," "intracellular organelle," "organelle membrane," and "vacuole" and returned at least one result from a PubMed fetch using either queries Q_FTD1 or Q_GRN2 (*See Methods: PubMed Fetching*). Two well-known examples are lysosomal cysteine proteases cathepsin Z (CTSZ) and cathepsin B (CTSB) which are reported to be upregulated and to show altered enzymatic activity in *GRN*-deficiency [36, 38,

67]. These data agree with the literature showing CTSZ to be significantly upregulated in MEF KO and showing CTSB to be significantly upregulated in iPSC KO. A newer example is CYLD lysine 63 deubiquitinase (CYLD) for which a recently discovered mutation p.M719V has been reported as causative for FTD and amyotrophic lateral sclerosis (ALS) [68]. The mutation results in hyperactive CYLD, a reduction in autophagosome fusion to lysosomes, and increased cytoplasmic accumulation of TDP-43 and fused-in-sarcoma [68, 69]. In these data, CYLD is only found in the MEF KO condition.

"Cellular response to stress" is shared by MEF WT, MEF KO, and iPSC-microglia WT but not iPSC-microglia KO. This is most interesting for the iPSC-microglia which, being an immune cell model, respond to signals of cellular stress and engage in either proinflammatory or anti-inflammatory actions depending on the stimulus [70]. This term's significance in solely iPSC-microglia WT but not iPSC-microglia KO highlights the downregulation of proteins in this pathway in *GRN*-deficiency. One of these proteins is interferon regulatory factor 3 (IRF3), a transcription factor that reduces neuroinflammation through activating response genes to suppress class II major histocompatibility complex activity, decrease proinflammatory cytokines, and increase anti-inflammatory cytokines [71]. Interestingly, TSPO is also a gene contributing to this pathway in iPSC-microglia WT.

Figures 10-13 show the top twenty pathways for each subset ordered by significance after filtering out GO terms at level 2. These figures highlight some unique pathways overrepresented in different subsets in addition to pathways shared with other subsets.

The MEF WT subset showed several significant pathways related to cholesterol metabolism and biosynthesis and lipid metabolism across multiple databases, indicating that *GRN*-deficiency results in decreased expression of proteins involved in cholesterol and lipid dynamics. This is supported by findings showing increases in total cholesterol and triglycerides (TGs) in the blood of FTD patients [43, 72-74] along with a finding showing increases in TGs with concomitant decreases in digycerides (DGs) and altered levels of cholesterol esters in *Grn* KO MEFs [42]. Evers et al. 2017 also found that cases of FTD due to *GRN* mutations could be distinguished from non-*GRN* related FTD, Alzheimer's disease, and

controls by the lipidomic signature of postmortem human brain tissue. One group found that aged or ovalbumin-challenged *Grn*$^{-/-}$ mice showed neuronal accumulation of GM2 ganglioside lipids [28], a subgroup of sphingolipids and substrates of HexA [75]. Complementing the accumulation of lipid species, models of *GRN*-deficiency demonstrate reduced levels of lipid metabolism and lipid catabolism proteins [42, 67] and reduced lysosomal glycosphingolipid enzyme activity [30, 41, 76, 77].

Notable proteins constituting the cholesterol-related pathways represented in the MEF WT subset include 3-hydroxy-3-methylglutaryl-CoA synthase 1 (HMGCS1) and low-density lipoprotein receptor (LDLR). HMGCS1 is an enzyme involved in a rate-limiting step of the isoprenoid pathway [78] while LDLR is a surface receptor that binds extracellular cholesterol and traffics it to the lysosome [79]. Interestingly, their mRNAs are bound by TDP-43, and cytoplasmic accumulation of TDP-43 has been found to reduce expression of HMGCS1 and cause LDLR to co-aggregate with TDP-43 in oligodendrocytes of FTD patients, resulting in disruption in cholesterol biosynthesis and uptake [80]. MEF KO cells only aggregate cytoplasmic TDP-43 in response to ubiquitin-proteosome system inhibition [81], however, and TDP-43 is not significantly differentially expressed in MEFs in these data. Therefore, TDP-43 pathology likely does not contribute to the reduced expression of HMGCS1 or LDLR in MEF KO in these data. The lysosomal lipid metabolizing enzymes lysosomal acid lipase (LIPA) and acid ceramidase (Asah-1), also known as acid sphingomyelinase-1 or N-acylsphingosine amidohydrolase-1, are both overexpressed in MEF WT. LIPA is crucial for hydrolyzing TGs and cholesterol esters [82] while Asah-1 digests glucosylceramide into glucosylsphingosine [83] and was recently found by us to be significantly decreased in *Grn*$^{-/-}$ mouse brain lysate [67]. In sum, these data and the literature strongly suggest that MEF KO cells model the accumulation of lipids that occurs in FTD.

The MEF KO subset showed a unique motif of "metabolism" in its top overrepresented pathways across multiple databases with specific pathways relating to mitochondrial compartments or mitochondria-related functions. The GO cellular compartment "mitochondrion" pathway (**Figure 6**) even ranked as more significant than "organelle"-related pathways despite the known association between

GRN-deficiency and lysosome dysfunction [66]. Disruption of mitochondrial transport and mitochondrial activity is implicated in the pathogenesis of several other neurodegenerative diseases like Alzheimer's disease, Parkinson's disease, ALS, and Huntington's disease [84]. Models of FTD due to mutations in c9 open reading frame 72 (c9orf72), the most common type of familial FTD [85], demonstrate mitochondrial dysfunction [86], and mutations in TDP-43 have been found to disrupt mitochondrial fission and fusion dynamics, disrupt mitochondrial trafficking, and to affect overall cellular bioenergetics although the precise mechanism for this behavior is unknown [87, 88].

Pertaining to FTD due to *GRN* mutations, recently $Grn^{-/-}$ mice showed reduced cerebral glucose metabolism as measured by fluorodeoxyglucose-µPET scan [51]. Additionally, primary cortical neurons from $Grn^{-/-}$ mice demonstrated increases in caspase-mediated apoptosis [81], the caspase system being one of the mitochondrial-driven methods of initiating apoptotic cell death in response to some cellular stressor [89]. Kleinberger et al. 2010 also showed both cytoplasmic accumulation of TDP-43 and increases in apoptosis in MEFs after ubiquitin-proteosome system inhibition. Indeed, "regulation of cell death," "positive regulation of cell death," and various stress response pathways are overrepresented in MEF KO. A notable gene overexpressed in MEF KO and constituting several of these pathways is Rab32 ($\log_2$ fold-change = 3.15; q = 0.0245). Rab32 regulates apoptosis through the targeting of protein kinase A to mitochondrial and endoplasmic reticulum (ER) membranes and influencing calcium handling by the ER [90]. Bui et al. 2010 found overexpression of Rab32 to shorten neurite length, alter mitochondrial morphology, and accelerate apoptosis. Overall, these data are supported by the literature and suggest that MEF KO cells may model mitochondrial dysfunction present in FTD possibly through pathways that influence cell death.

Pathways unique to the iPSC-microglia WT subset centered around RNA metabolism and processing, ribonucleoproteins, and nucleus-adjacent cellular compartments. These results indicate that proteins constituting these pathways are underrepresented in iPSC-microglia KO. In the literature, RNA metabolism dysfunction and altered ribonucleoprotein (RNP) dynamics are well-known features of ALS

and FTD [91]. Indeed, mutations in several RNA binding proteins including TDP-43, FUS, TATA-box binding protein associated factor-15, Ewing sarcoma breakpoint region-1, heterogenous nuclear ribonucleoproteins A1/A2, and Tia1 cytotoxic granule-associated RNA binding protein (TIA1) are linked to sporadic and familial cases of ALS and FTD. Mutations in these proteins result in their aggregation in their respective neuronal cell types [92]. These RNA binding proteins are recognized by proteins in the protein quality control (PQC) system like c9orf72, valosin-containing protein, p97, sequestosome-1 (SQSTM1)/p62, nucleoporin 62, and optineurin-1 (OPTN1) which attempt to clear them [93]. Interestingly, mutations in these PQC system proteins also result in ALS and FTD, functionally connecting RNA metabolism and the PQC system under ALS and FTD [91]. Apart from TIA1 (**Table 3**), none of the above-mentioned RNA-binding proteins nor PQC proteins are significant in these data. However, the PQC system cooperates with and overlaps with autophagy [91, 94], which is known to be disrupted in *GRN*-deficiency [33, 67, 95]. In these data, proteins like ubiquitin specific peptidase-8, programmed cell death-11, ubiquitin conjugating enzyme E2 E1, and ubiquitin protein ligase E3C are upregulated in iPSC-microglia WT suggesting possible dysfunction in the PQC machinery in iPSC-microglia KO.

The role of RNA metabolism in FTD and ALS is largely driven cytoplasmic accumulation of TDP-43 which occurs with both mutations in TDP-43 and mutations in other RNA binding proteins [91]. TDP-43, as an RNA binding protein, plays a direct role in the splicing, translation, and degradation of mRNA [96, 97]. Pathological TDP-43 disrupts RNA processing and disrupts normal transport between the cytoplasm and the nucleus through sequestration of nucleoporins, RNPs, and other nucleocytoplasmic machinery [98, 99]. Pathological TDP-43 can be recruited to stress granules, which are membrane-less organelles that form naturally in response to stress to sequester RNA, RNPs, and other cytoplasmic proteins and are sites of RNA metabolism [100, 101]. The presence of TDP-43 or other RNA-binding proteins like TIA1, expressed roughly four times higher in iPSC-microglia KO (**Table 3**), in stress granules slows the disassembly of the stress granule and can lead to an aggregate-like state, shunting them

to the ubiquitin-proteosome system to be degraded [91]. Large stress granules can overwhelm the ubiquitin-proteosome system and fail to be degraded, inhibiting anterograde transport in neurons [102]. Whether PGRN's implication in neurite outgrowth is explained by this mechanism remains to be determined. While TDP-43 is not significantly differentially expressed in the iPSC-microglia nor are there explicit "stress granule" pathways overrepresented in either subset, stress granules, RNA-related processes, and autophagy are tightly related in ALS and FTD. Given that stress granules can form in microglia [103], the future observation of stress granules in the iPSC-microglia cell model may explain the overrepresentation of several RNA-related pathways in the iPSC-microglia WT.

The iPSC-microglia KO subset enriched pathways related to the secretion of extracellular vesicles. The secretion of vesicles is a well-known phenomenon of several cell types including central nervous system cells like neurons, astrocytes, oligodendrocytes, and microglia, with these vesicles having been categorized into distinct subtypes based on their size and contents [104, 105]. Regardless of typical function, activated microglia shed more vesicles, often containing cytokines or other inflammatory markers. Additionally, lysosome dysfunction has been found to upregulate exocytosis and vesicle secretion in microglia [106]. The overrepresentation of secretion-related pathways in the iPSC-microglia KO is supported by literature suggesting that *GRN*-deficient microglia are more active, more inflammatory, and demonstrate lysosome dysfunction [37, 38, 51-54]. Moreover, culturing primary thalamic mouse neurons with conditioned media from $Grn^{-/-}$ microglia was sufficient to induce TDP-43 granule formation, nuclear pore defects, and cell death in those neurons, operating primarily through complement proteins C1qA and C3 [107]. While these reports did not specifically mention secreted vesicles, they demonstrate that secreted complement proteins from *Grn*-deficient microglia are sufficient to induce FTD hallmarks. In these data, C1qA was not significantly differentially expressed in the iPSC-microglia and C3 was not found, but complement protein C1qB, a similar subunit of C1q, was significantly higher in the iPSC-microglia KO ($\log_2$ fold-change = 1.62; q = 0.0109). Additionally, CTSB, a lysosomal enzyme commonly found in vesicles secreted from microglia [108], is upregulated in iPSC-

microglia KO (log_2 fold-change = 1.23; q = 0.00415). Altogether, the significant overrepresentation of "secretion"-related pathways along with the overrepresentation of "lysosome" and "lysosome"-adjacent pathways (**Supplemental Table 1**) indicates that the iPSC-microglia KO show lysosome dysfunction and increases in inflammation which is supported by the literature.

Conclusion

Overall, this work is a thorough effort to identify shared and unique features across different models of *GRN*-deficiency using quantitative proteomics. While some pathways are shared, and others are unique to specific subsets, these features converge to produce a holistic view of FTD due to *GRN* mutations.

These data, supported by the literature, suggest that *GRN* pathology is driven by dysfunction in lysosomal lipid metabolism and catabolism resulting in the accumulation of lipids. All subsets demonstrated evidence of lysosome dysfunction through the overrepresentation of lysosome-related pathways. These results are grounded by the fact that PGRN is trafficked to the lysosome [20-22] and purported to interact with several lysosomal proteins [23-29, 40]. Recent hypotheses center on the primary pathogenic mechanism of *GRN*-deficiency being decreased levels of lysosomal PSAP due to a loss in co-trafficking of PGRN and PSAP [77, 109]. Reduced lysosomal PSAP reduces saposin levels, the peptides making up PSAP [110], which are crucial cofactors for several glycosphingolipid metabolizing enzymes [111]. PGRN may also directly interact with cathepsin D (CTSD). The role of this interaction on lipid metabolism is unknown; however, mutations in the *CTSD* gene, like *GRN*, cause a subtype of NCL and result in the accumulation of lipofuscin [112], suggesting there may be a direct role. The reduction in lysosomal PGRN and PSAP in *GRN*-deficiency disrupts lysosomal proteolytic activity and results in the accumulation of lipids which indirectly affects other cellular processes.

This idea is supported by findings that lipid species are altered in *GRN*-deficient brain tissue and plasma [42, 43, 72-74], lipid metabolizing proteins show decreased expression [42, 67], and lipid-digesting enzymes show decreased activity [30, 41, 76, 77]. Recently lipids, including glycerolipids (*e.g.*, TGs, DGs), phospholipids, ceramides, and cholesterol esters, were found to accumulate in $Grn^{-/-}$ microglia in the form of lipid droplets (LDs) [45]. These $Grn^{-/-}$ microglia shared several features with

lipid droplet-accumulating microglia that occur with age, including altered lysosomal and immune-related gene expression and increased expression of cytokines both at baseline and in response to stress.

In these data, the MEF WT subset demonstrated the strongest association with lipid metabolism through its several cholesterol- and lipid-related pathways along with overexpression of proteins like LDLR, HMGCS1, Asah-1, and LIPA. While LDs are commonly degraded in peroxisomes or mitochondria, they can also be degraded through trafficking to lysosomes, a process call lipophagy [113, 114]. Reduced lipophagy because of dysfunction in lysosomal lipid metabolism can seed the accumulation of lipids in the cell. Evers et al. 2017 found *Grn* KO MEFs to accumulate TGs and some cholesterol esters which are lipids commonly found in LDs. Lipid accumulation can disrupt mitochondrial function by increasing reactive oxygen species [45, 114, 115], which may correspond to the overrepresentation of mitochondria- and metabolic-related pathways as well as pathways like "regulation of cell death" and "regulation of response to oxidative stress" in the MEF KO subset (**Figure 11**). Moreover, some lysosome-derived metabolites are transferred to the mitochondrial matrix to be used in the tricarboxylic acid cycle [116], so lysosome dysfunction that affects metabolite transfer to the mitochondria would also affect mitochondrial function. Altogether, this suggests that the primary dysfunctional phenotype in *Grn* KO MEFs is the dysregulation of lipid metabolism resulting in the accumulation of lipids and the disruption of both lysosomal and mitochondrial function.

Interestingly, these data also suggest that lipid metabolism plays a role in the iPSC-microglia model. While the primary feature of the iPSC-microglia KO subset is pathways related to secretion of vesicles, "regulation of lipid storage" is also a significant pathway being constituted by proteins like perilipin-2 (PLIN2) ($\log_2$ fold-change = 2.79; q = 0.0165) and carnitine palmitoyltransferase-1A (CPT1A) ($\log_2$ fold-change = 3.39; q = 0.0000188). PLIN2 is a LD surface protein and was found to be increased in aged lipid droplet-accumulating microglia and $Grn^{-/-}$ microglia [45] while CPT1A is a mitochondrial, fatty acid oxidation enzyme [117]. Their overexpression in iPSC-microglia KO may represent increased numbers of LD's and a cellular response to increased lipid levels, respectively. Moreover, the

overrepresentation of secretion-related pathways may be an indication of an inflammatory state in the iPSC-microglia KO subset [105] possibly generated by lipid accumulation, a well-known phenomenon [44, 114]. The increase in vesicle secretion may be an attempt by the iPSC-microglia KO cells to secrete lipids and alleviate some of the burden. This is a strategy used by neurons to reduce the stress from toxic inclusions like amyloid-β plaque, tau, and mutant super oxide dismutase [104, 105] but also has been used by neurons to reduce the stress of lysosomal cholesterol accumulation in Niemann-Picks disease [118]. Cholesterol efflux is also a common mechanism to reduce inflammation in the cardiovascular system [119, 120].

Across the two cell types, there were several conserved significant pathways (**Table 2; Supplemental Table 1**). However, these pathways arose through different significant proteins as only 23 proteins were significant between both cell types (**Table 1**). Many proteins are significant in one cell type but do not meet the significance criteria in the other cell type. Sometimes, these nonsignificant proteins have very low q-values but fail to meet the fold-change criterium, indicating less robust but perhaps meaningful expression differences. This occurred with some proteins known to be upregulated in *GRN*-deficiency like CTSD which had a $\log_2$ fold-change of 0.734 (q = 0.000184) in the iPSC-microglia. Similarly, CTSB is reported to be upregulated in *GRN*-deficiency [121], but it did not meet the fold-change criterium ($|\log_2$ fold-change$| > 1.0$) in the MEFs with a $\log_2$ fold-change of 0.354 (q = 0.0128).

Interestingly, some proteins are significant in one genotype of a cell model yet are significant in the opposite genotype of the other cell model (**Table 1**). This may be a result of a cell-type-specific difference, random chance, or even a spurious result of mass spectrometry methods such as a mis-quantification of a peptide or the erroneous mapping of a peptide to a protein. CTSD is a topical example. Although it did not reach significance in either cell type, CTSD is trending in opposite directions between the two cell types with a $\log_2$ fold-change of 0.734 (q = 0.000184) in the iPSC-microglia and a $\log_2$ fold-change of -0.869 (q = 0.000764) in the MEFs. Unpublished results from our lab (*data not shown*) along with literature [24, 27, 34, 37, 121] suggest that CTSD should be upregulated in MEF KO, contrasting

with these data. Regardless of the reasons why some proteins show opposing expression across the cell types, this feature of the data underscores the importance of verifying proteomic data in the lab.

Importantly, these analyses have some clear limitations. Firstly, they are limited by the relatively low number of replicates, having only three replicates per MEF genotype and only five replicates of iPSC-microglia WT and four replicates of iPSC-microglia KO. Secondly, they suffer from the typical limitations of ORA as opposed to a network-based analysis approach [122]. In ORA, proteins are designated as significant using some cutoff criteria, and then those proteins are used for ORA via a count-based hypothesis test; here, I used Fisher's Exact Test with exact rather than estimated p-values. This procedure eliminates proteins which may show small but meaningful differences between groups. Additionally, within the set of significant proteins, the fold-change values are ignored, and all proteins are treated equally without considering the implication of one protein being considerably more differentially expressed than another. Finally, ORA assumes both that each protein is independent of all other proteins and that each pathway is independent of other pathways.

Despite these limitations, this work produces insight into the pathology of FTD due to *GRN*-deficiency through the analysis and comparison of two different cell models of *GRN*-deficiency. These results are corroborated by literature findings, and in turn, these analyses support the hypothesis that *GRN*-deficiency produces dysfunction in lysosomal lipid metabolism and catabolism resulting in the accumulation of lipids. This work is strengthened by the use of the random forest algorithm, strongly supported by the literature for these data [47], to impute missing values. Moreover, the accuracy of the algorithm was tested empirically and was found to be quite effective with all estimated error rates less than 0.11.

Importantly, this work highlights the strengths of each cell model in studying *GRN*-deficiency. These data and the literature demonstrate that cholesterol and lipid metabolism are disrupted in *Grn* KO MEFs [42] (**Figure 11**). These results along with the fact that MEF cells endogenously synthesize most lipids [42] makes them an excellent candidate cell model for studying lipid metabolism and lipid

accumulation in *GRN*-deficiency. Additionally, these and future MEF proteomic data can be compared to other published proteomic datasets such as one from mouse liver lysosomes [123] or one from MEF lysosomes [124]. Microglia are a highly relevant cell type in FTD being the cell type that expresses the most PGRN in the CNS [16]. Moreover, microglia are suggested to play a crucial role in the pathogenesis of FTD [37, 38, 45, 54, 107]. These analyses identify pathways related to RNA dynamics and secretion of vesicles as being overrepresented in iPSC-microglia WT and iPSC-microglia KO, respectively, (**Figure 7**) and pathways related to lysosome dysfunction being overrepresented in both (**Supplemental Table 1**). Additionally, the upregulation of PLIN-2 and the overrepresentation of the "regulation of lipid storage" pathway in iPSC-microglia KO suggest that lipid accumulation may occur in this subset. These data suggest future endeavors using this model should include determining the effect of conditioned media from iPSC-microglia KO on other cell types and include the study of stress granules or lipid droplets in iPSC-microglia KO.

Methods

Cell pellet digestion.

Three replicates of MEF *Grn* WT and *Grn* KO cells were lysed 300 µL of urea lysis buffer (8 M urea, 10 mM Tris, 100 mM NaH_2PO_4, pH 8.5), including 3 µL (100x stock) HALT(-EDTA) protease and phosphatase inhibitor cocktail (Pierce) was added to the cell pellets. Samples were sonicated (Sonic Dismembrator, Fisher Scientific) 3 times for 5 sec each with 5 sec intervals of rest at 25% amplitude to disrupt nucleic acids and were subsequently centrifuged at 4° C. Protein concentration was determined by the bicinchoninic acid (BCA) method, and samples were frozen in aliquots at -80 °C. Protein homogenates (100 µg) were treated with 1 mM dithiothreitol (DTT) at room temperature for 30 min, followed by 5 mM iodoacetimide at room temperature for 30 min in the dark. Protein samples were digested with 1:100 (w/w) lysyl endopeptidase (Wako) at room temperature for overnight. Next day, samples were diluted with 50 mM NH_4HCO_3 to a final concentration of less than 2 M urea and were further digested overnight with 1:50 (w/w) trypsin (Promega) at room temperature. Resulting peptides were desalted with HLB column (Waters) and were dried under vacuum.

Five replicates of *GRN* WT iPSC-derived microglia and four replicates of *GRN* KO iPSC-derived microglia were lysed in urea lysis buffer (8M urea, 100 mM NaHPO4, pH 8.5), including 5 uL (100x stock) HALT protease and phosphatase inhibitor cocktail (Pierce) by repeated pipetting. Protein supernatants were transferred to new 1.5 mL Eppendorf tubes and sonicated (Sonic Dismembrator, Fisher Scientific) 3 times for 5 s with 15 s intervals of rest at 30% amplitude to disrupt nucleic acids and subsequently vortexed. Protein concentration was determined by the bicinchoninic acid (BCA) method, and samples were frozen in aliquots at −80°C. The samples (100ug) were then treated with 1 mM (final concentration) dithiothreitol (DTT) at 25°C for 30 minutes. This was followed by 5 mM (final concentration) iodoacetimide (IAA) at 25°C for 30 minutes in the dark. The samples were then digested with 1:100 (w/w) lysyl endopeptidase (Wako) at 25°C for 4 hours and then diluted with 50 mM NH4HCO3 to a final concentration of less than 2M urea. Trypsin (Promega) was added at 1:50 (w/w) and digestion was allowed to proceed overnight. Resulting peptides were desalted with a Sep-Pak C18 column (Waters) and dried under vacuum.

MS data acquisition.

The data acquisition by LC-MS/MS protocol was adapted from a published procedure [125] and was performed by the Integrated Proteomics Core Facility at Emory University for both cell types.

MEF-derived peptides were resuspended in 100 µL loading buffer (0.1% trifluoroacetic acid). Peptide mixtures (2 uL) were separated on a self-packed C18 (1.9 µm, Dr. Maisch, Germany) fused silica column (30 cm x 75 µm internal diameter (ID); New Objective, Woburn, MA) attached to an EASY-nLC™ 1200 system and were monitored on a Q-Exactive HF-X Mass Spectrometer (ThermoFisher Scientific, San Jose, CA). Elution was performed over a 90 min gradient at a rate of 300 nL/min (buffer A: 0.1% formic acid in water, buffer B: 0.1 % formic acid in acetonitrile): The gradient started with 1% buffer B, went to 7% in 3 minutes, then increased from 7% to 35% in 67 minutes, then to 90% within 5 minutes and finally staying at 90% for 15 minutes. The mass spectrometer cycle was programmed to collect one full MS scan followed by 20 data dependent MS/MS scans. The MS scans (400-1600 m/z range, 3x106 AGC target, 100 ms maximum ion time) were collected at a resolution of 120,000 at m/z 200 in profile mode. The HCD MS/MS spectra (1.6 m/z isolation width, 30% collision energy, 1x105 AGC target, 86 ms maximum ion time) were acquired at a resolution of 7,500 at m/z 200. Dynamic exclusion was set to exclude

previously sequenced precursor ions for 20 seconds within a 10-ppm window. Precursor ions with unassigned, and +7, or higher charge states were excluded from sequencing.

iPSC-microglia-derived dried peptides were reconstituted in 100 uL of loading buffer (0.1% formic acid, 0.03% TFA, 1% acetonitrile). Each sample (2uL) was loaded onto and eluted from a self-packed C18 fused silica column (25 cm x 75 uM internal diameter (ID); New Objective, Woburn, MA) driven by Thermo Easy-nLc 1200 ultra-high liquid chromatography system coupled to a Fusion Lumos mass spectrometer (ThermoFisher Scientific, San Jose, CA). Elution was performed over a 120-minute gradient at a rate of 250nl/min with buffer B ranging from 3% to 35% (buffer A: 0.1% formic acid in water, buffer B: 0.1 % formic in 80% acetonitrile). The mass spectrometer cycle was programmed to collect at the top speed for 3 second cycles with higher-energy collision dissociation (HCD) fragmentation. The MS scans (200-1500 m/z range, 400,000 AGC, 50 ms maximum ion time) were collected at a resolution of 120,000 at m/z 200 in profile mode by the orbitrap while the HCD MS/MS spectra were captured by the ion trap (0.7 m/z isolation width, 30% collision energy, 10,000 AGC target, 35 ms maximum ion time) in centroid mode. Dynamic exclusion was set to exclude previous sequenced precursor ions for 20 seconds within a 10-ppm window.

MaxQuant:

Label-free quantification analysis was adapted from a published procedure [125]. MEF spectra were searched using the search engine Andromeda, integrated into MaxQuant (v. 1.6.1.0), against Mouse UniProt database (54,518 target sequences). Methionine oxidation (+15.9949 Da), asparagine and glutamine deamidation (+0.9840 Da) and protein N-terminal acetylation (+42.0106 Da) were variable modifications (up to five allowed per peptide); cysteine was assigned as fixed carbamidomethyl modification (+57.0215 Da). Only fully tryptic peptides with up to two miscleavages were considered in the database search. A precursor mass tolerance of ±20 ppm was applied before mass accuracy calibration and ±4.5 ppm after internal MaxQuant calibration. Other search settings included a maximum peptide mass of 6,000 Da, a minimum peptide length of six residues and 0.05-Da tolerance for high resolution MS/MS scans. The FDR for peptide spectral matches, proteins and site decoy fraction was set to 1%. Quantification settings were as follows: match full MS1 peaks between runs; use a 0.7-min retention time match window after an alignment function was found with a 20-min retention time search space. The LFQ algorithm in MaxQuant was used for protein quantitation. The quantitation method considered only razor and unique peptides for protein level quantitation.

iPSC-microglia spectra were processed through the MaxQuant pipeline (version 1.6.1.0) and searched against a Homo sapiens UniProt database supplemented with ApoE and Aβ specific sequences (90303 sequences downloaded April 2015). Search parameters included fully tryptic trypsin enzyme specificity with an allowance of 2 miscleavages, ±20 ppm precursor ion tolerance, 0.6 Da product ion tolerance, dynamic modifications for oxidized methionine (+15.9949 Da), asparagine and glutamine deamidation (+0.9840 Da), and static modification of carbamidomethylated cysteines (+57.0215 Da). All FDR settings were kept at the default of 1%, and “match between runs” was on.

Imputation

Data had missing values imputed using a random forest algorithm implemented in the R package MissForest [46].

The random forest algorithm was tested for accuracy empirically for each subset (MEF WT, MEF KO, iPSC-microglia WT, iPSC-microglia KO) using NRMSE as the error metric [48]. The following protocol was used. Proteins with actual missing values were filtered out of each subset producing the “filtered

subset." Then, each filtered subset had missing values artificially introduced at a proportion identical to the actual proportion of missing values in that original subset. Those missing values were imputed back with the random forest algorithm using ten iterations maximum, number of trees hyperparameter set to 100 or 500 trees, and bootstrap sampling a number of samples equal to the number of replicates. The estimated NRMSE, supplied by the algorithm, was collected and the true NRMSE was calculated comparing the imputed values to the original values. This protocol was performed twenty times for each subset and number of trees hyperparameter setting (100 or 500 trees) combination to produce forty total simulations per subset. Twenty simulations per subset per number of trees setting was chosen due to high computation times.

Following empirical testing of the random forest algorithm, each subset was imputed using the number of trees hyperparameter set to 100, ten iterations maximum, and bootstrap sampling a number of samples equal to the number of replicates.

Differential Expression Analysis

Differential expression was tested using unpaired T-tests assuming equal variances on proteins between MEF WT and MEF KO and between iPSC-microglia WT and iPSC-microglia KO. The p-values were corrected for multiple comparisons using FDR. P-value correction was performed separately for each cell-type. Significant proteins were those with a $\log_2$ fold-change > 1.0 and a q-value < 0.05.

Overrepresentation Analysis and GO Pruning

Overrepresentation analysis was performed on significantly different proteins using the R package gProfiler2 [57]. The Gene Ontology database used was updated as of 5/1/21.

The returned Gene Ontology pathways were filtered for nominal p-values of < 0.05 and then submitted for pruning using REVIGO [63]. The nominal p-values of those pathways were also submitted to weight the importance of pathways during the pruning process. REVIGO pruned GO pathways based on their semantic similarity using the *SimRel* formula [64] and the number of shared genes that constitute the pathway. Pathways sharing greater than 50% of genes with another more significant pathway were pruned. If the p-values for two pathways were close, the more general term was removed unless the terms were in a parent-child relationship in which case the child was removed.

The resulting unpruned pathways had their p-values corrected for multiple comparisons using the Holm method for the MEFs and the FDR method for the iPSC-microglia. Pathways were considered significant if they had a p-value < 0.01 for MEFs or a q-value < 0.01 for iPSC-microglia.

PubMed Fetching

The package easyPubMed [126] was used to help identify associations between proteins of interest and FTD or *GRN*. Protein names of interest (*e.g.*, proteins that constituted a particular significant pathway) were prepended to a PubMed query to create a unique query of each protein and that query. The *fetch_pubmed_ids()* and *get_pubmed_data()* functions were used to identify papers and pull their PubMed identifiers.

Queries referenced in this manuscript are in the table below where "*protein*" represents the protein name.

Name	Query String
Q_GRN1	"*protein* AND granulin"
Q_GRN2	"*protein* AND granulin[Title]"
Q_FTD1	"*protein* AND ((frontotemporal dementia[Title]) OR (frontotemporal lobar

	dementia[Title]))"

Figure 1

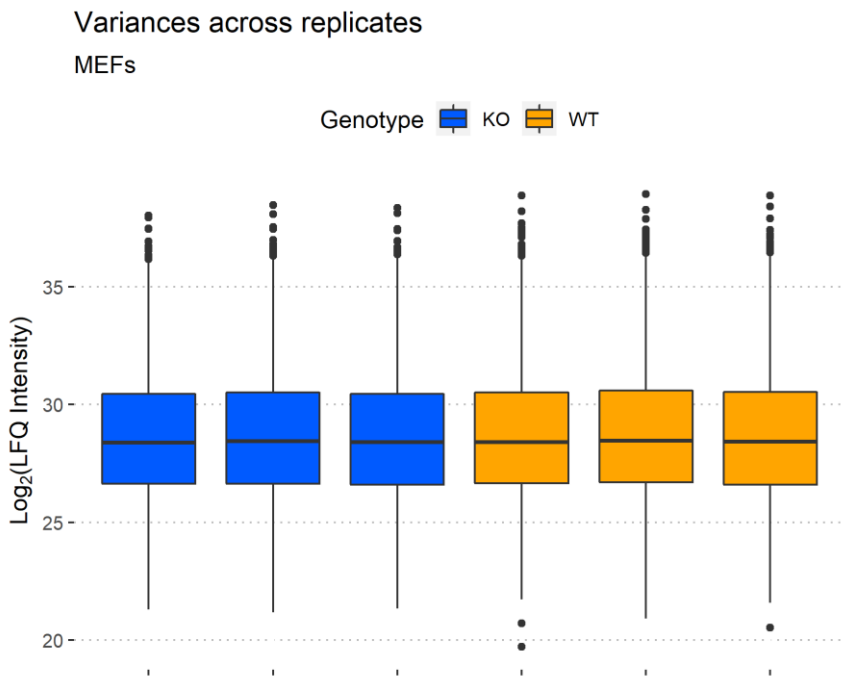

Figure 2

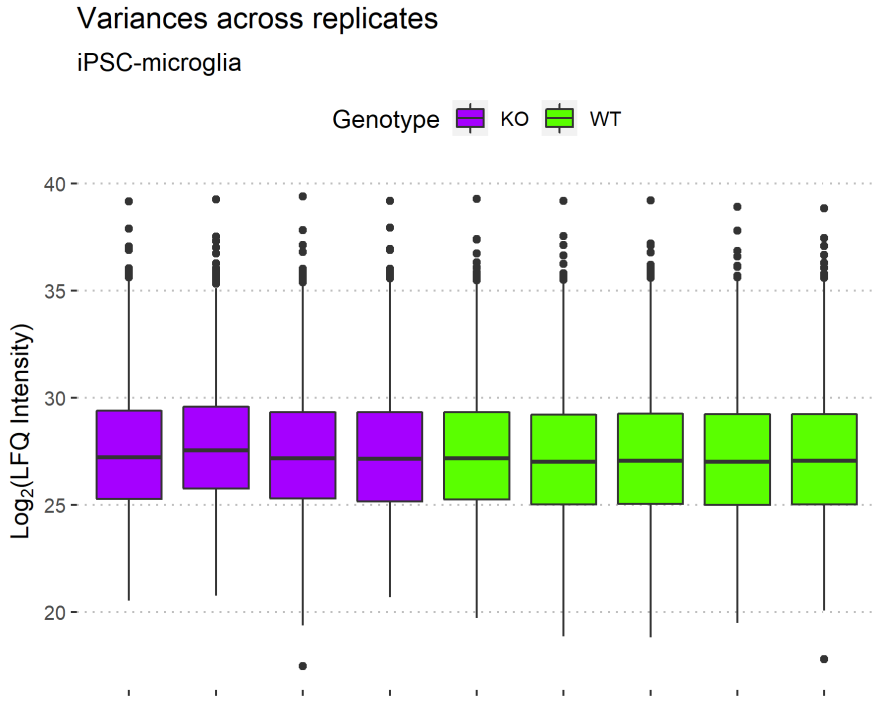

Figure 3

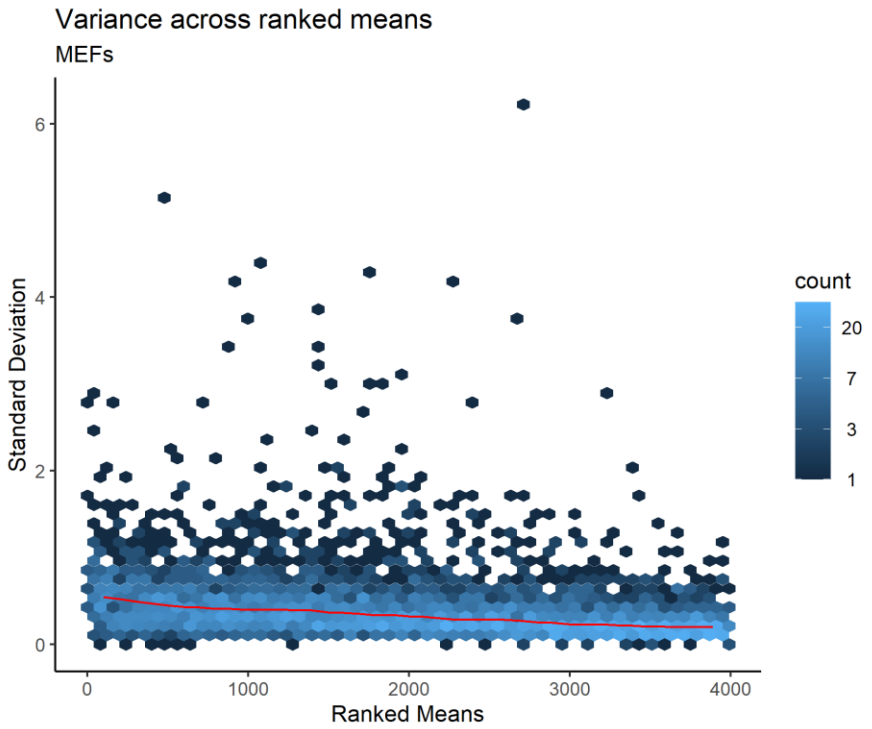

Figure 4

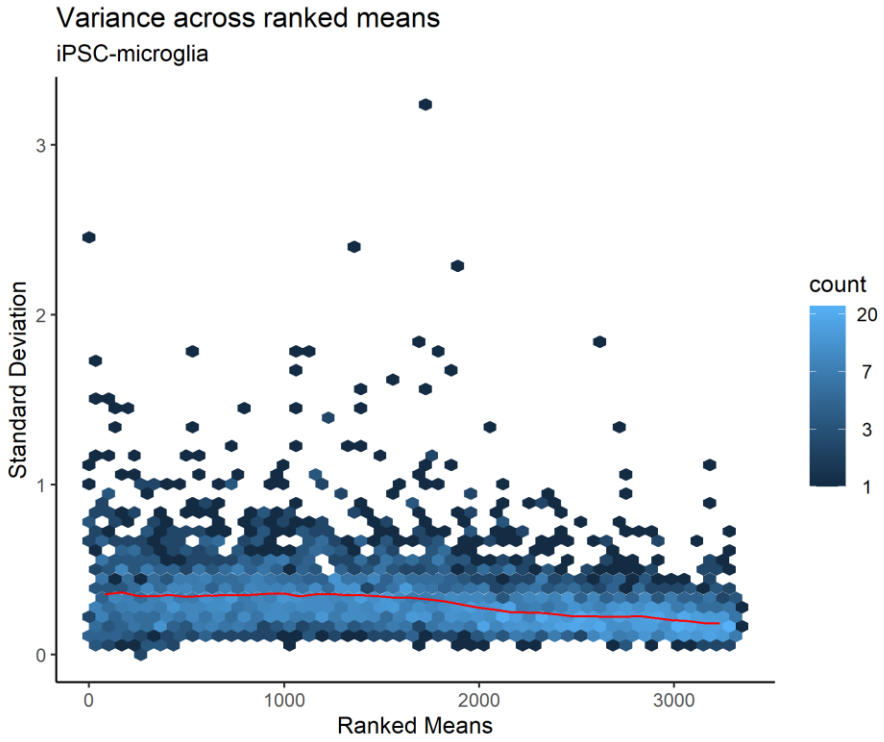

Figure 5

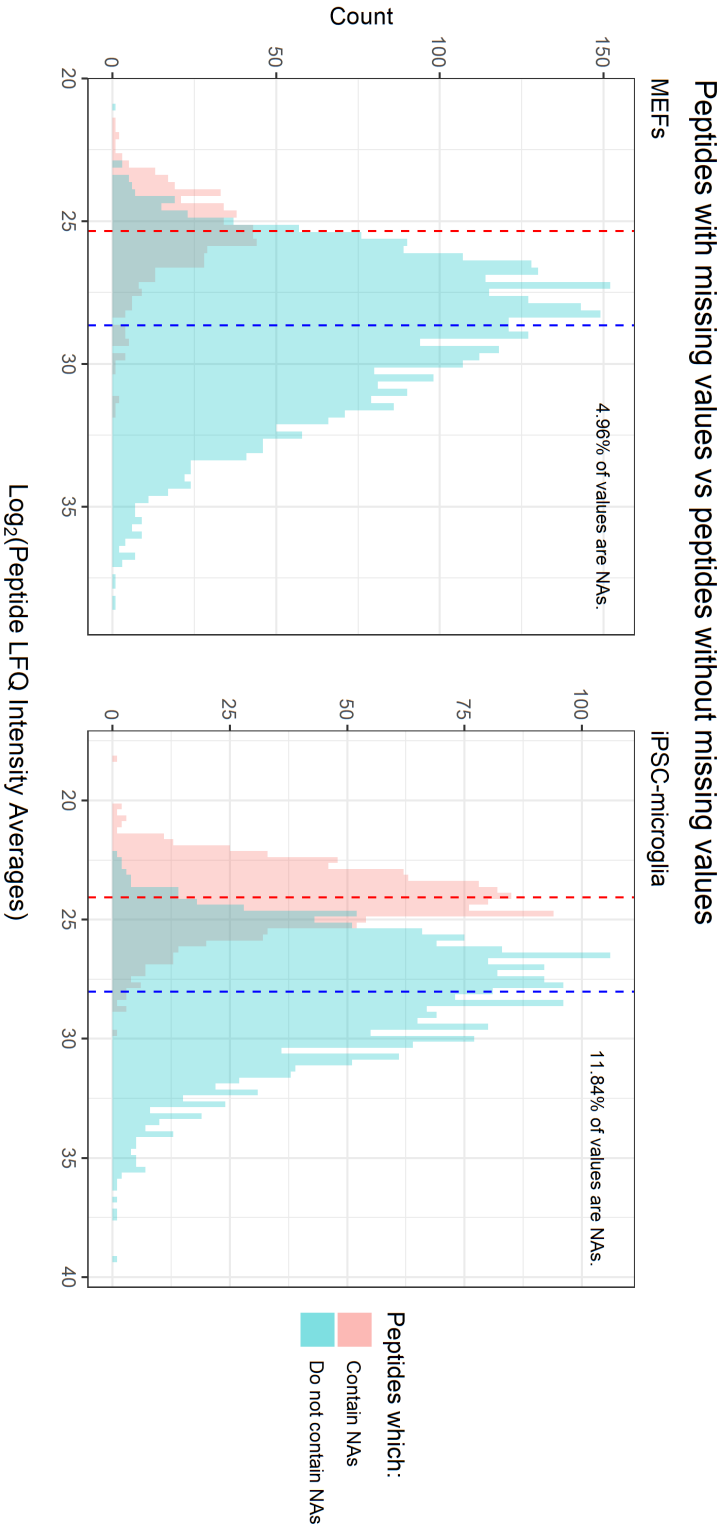
Peptides with missing values vs peptides without missing values
MEFs
iPSC-microglia
Count
4.96% of values are NAs.
11.84% of values are NAs.
Log2(Peptide LFQ Intensity Averages)
Peptides which:
Contain NAs
Do not contain NAs

Figure 6

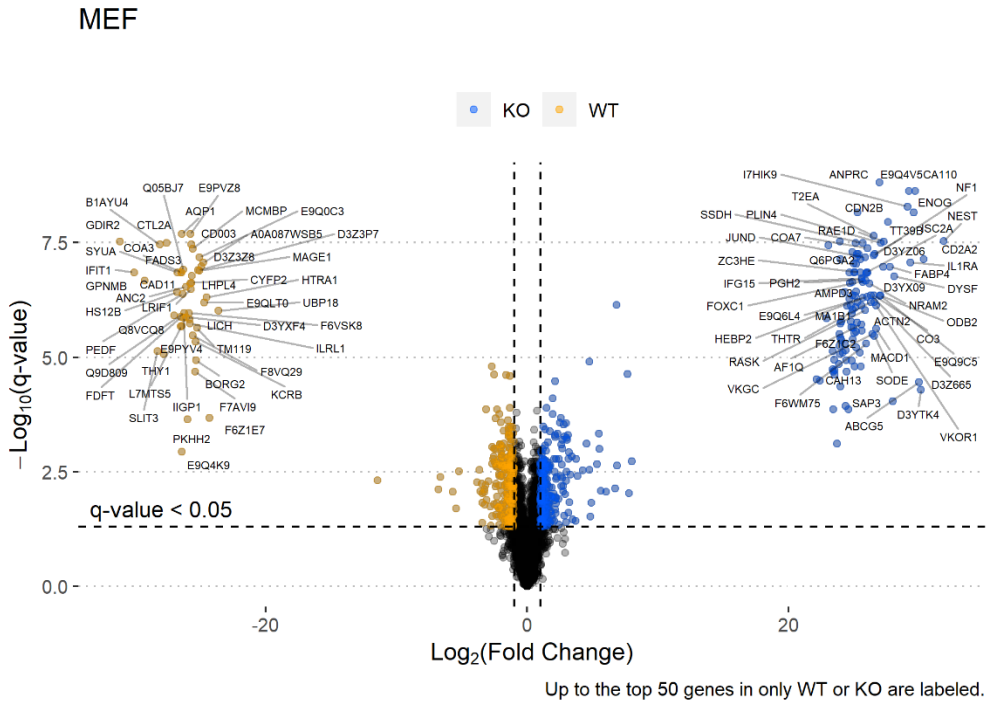

Up to the top 50 genes in only WT or KO are labeled.

Figure 7

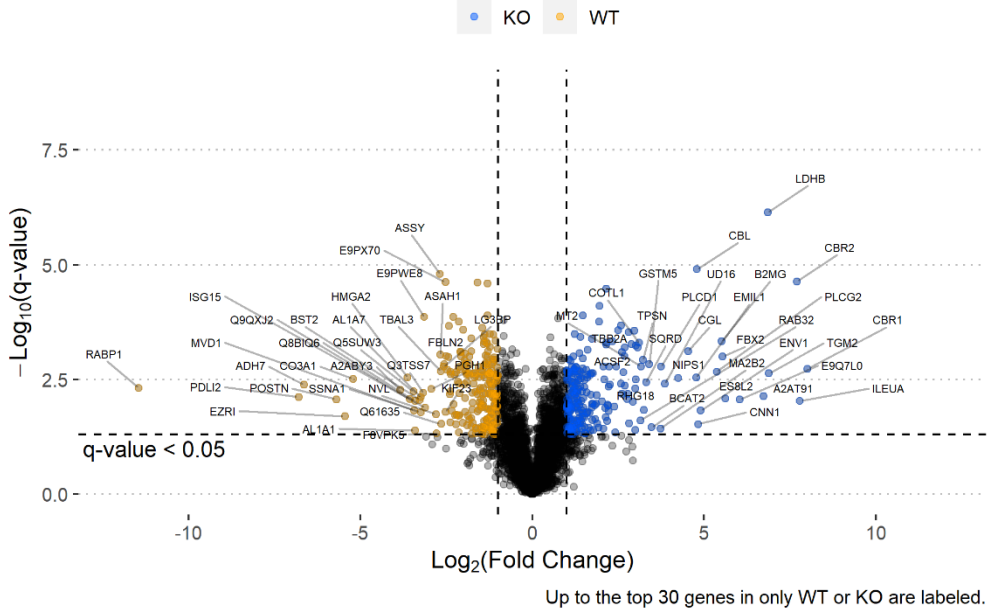

Up to the top 30 genes in only WT or KO are labeled.

Figure 8

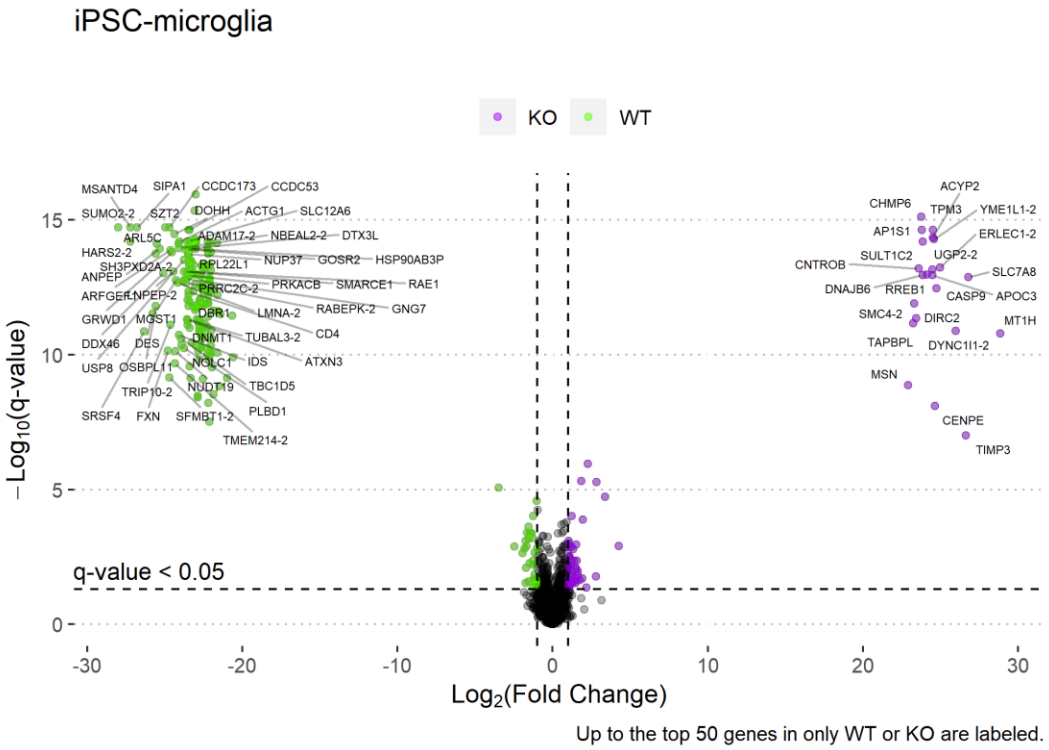

Figure 9

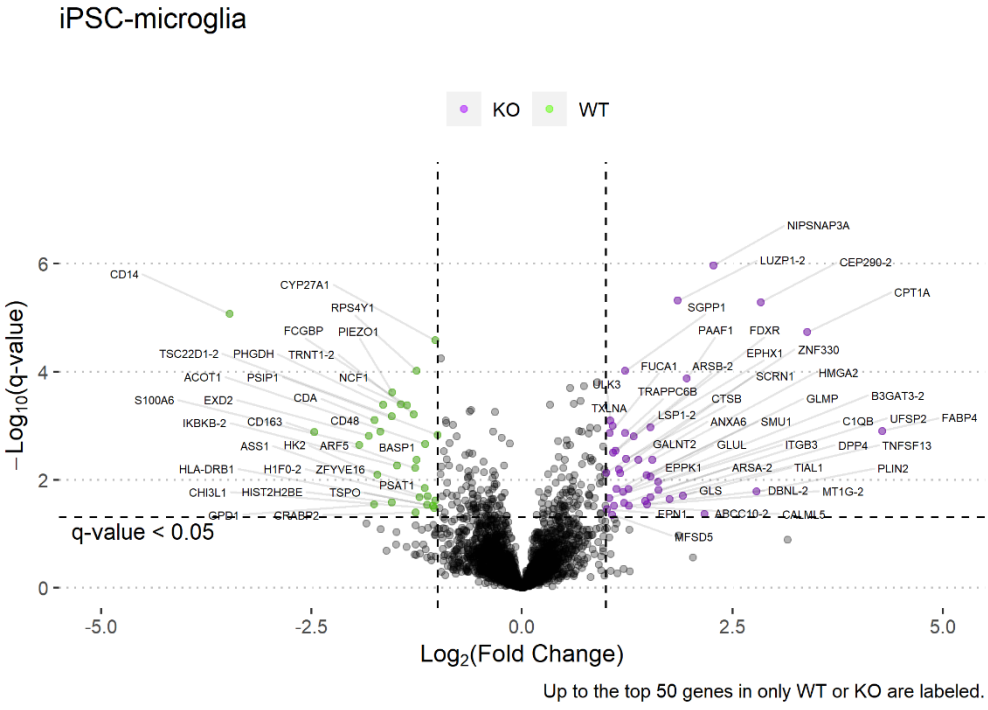

Figure 10

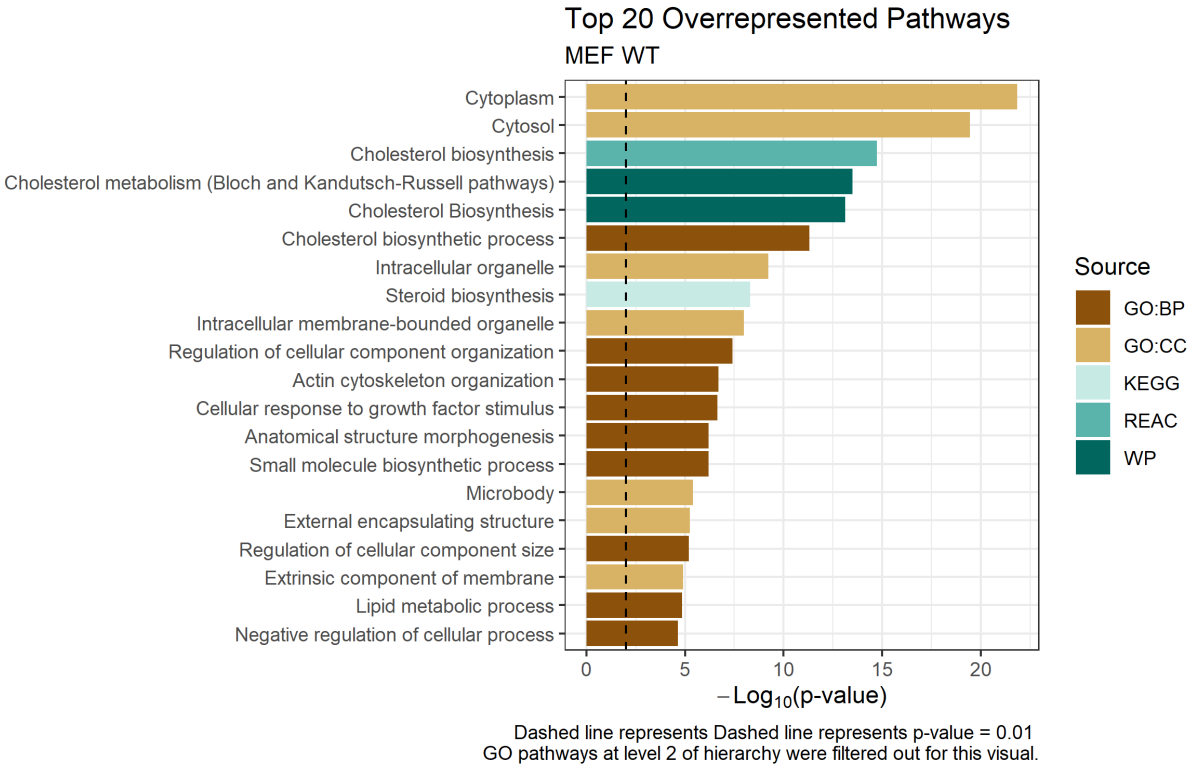

Figure 11

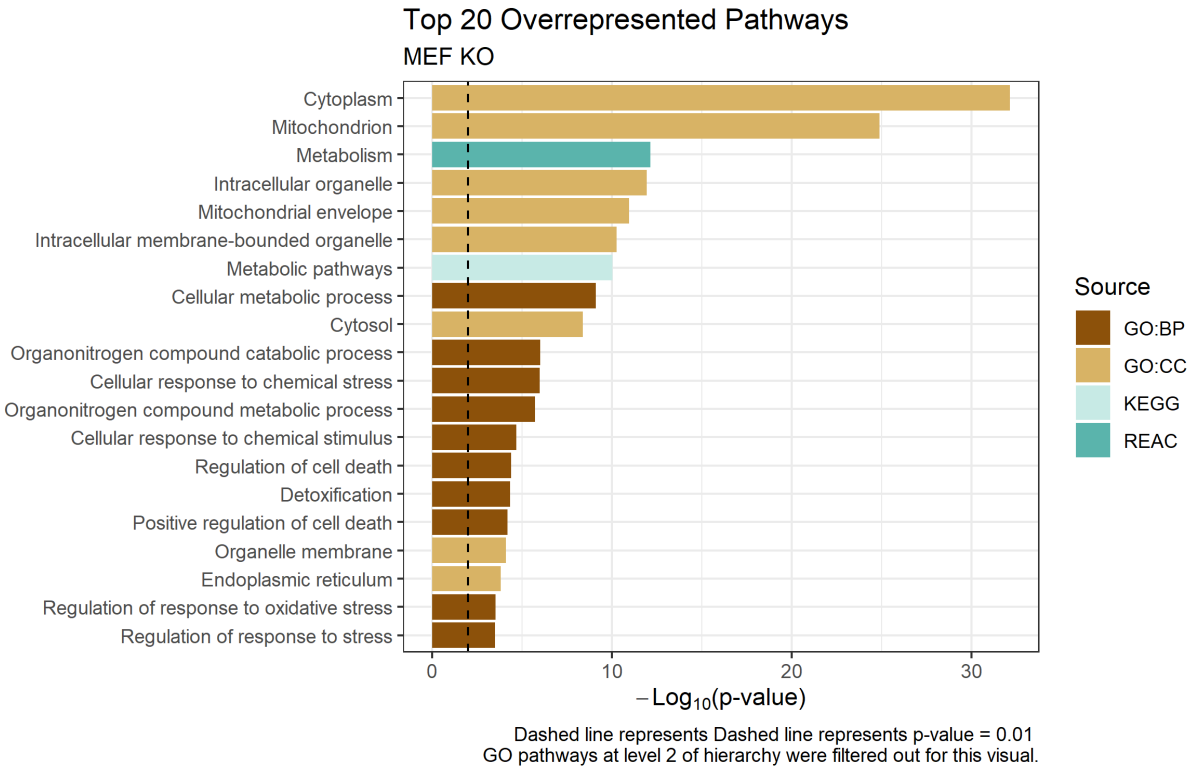

Figure 12

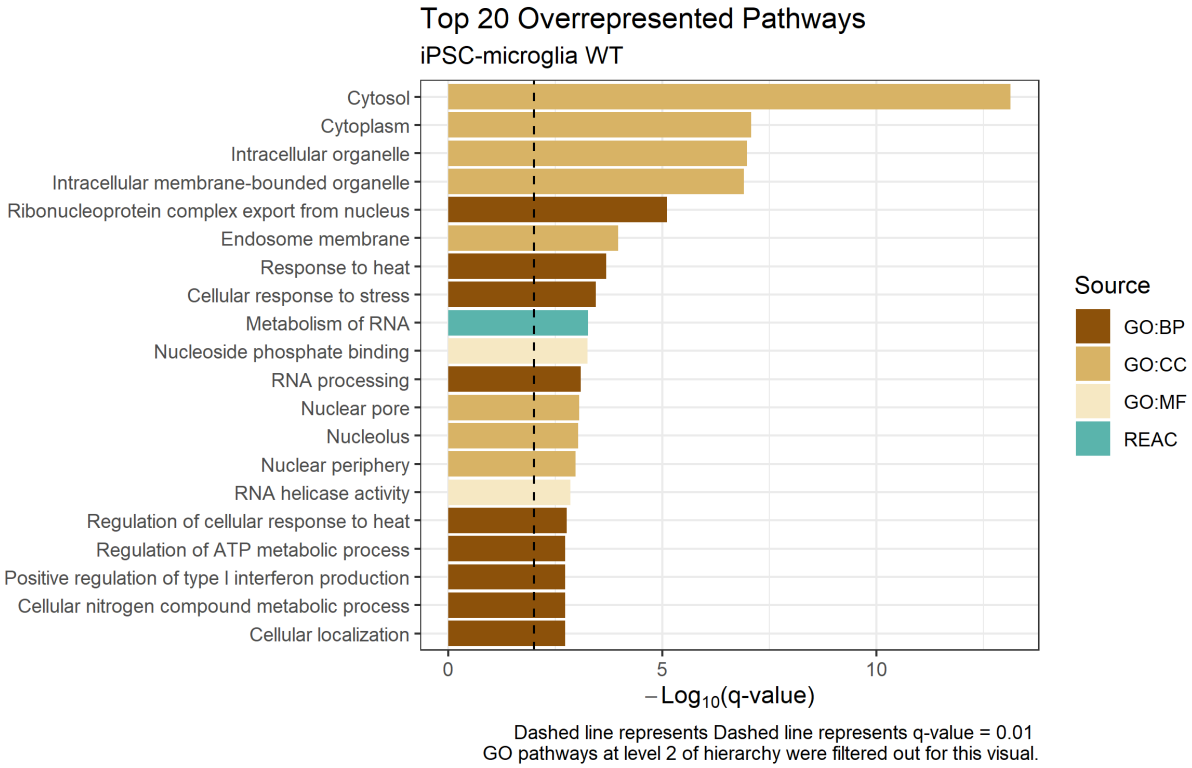

Figure 13

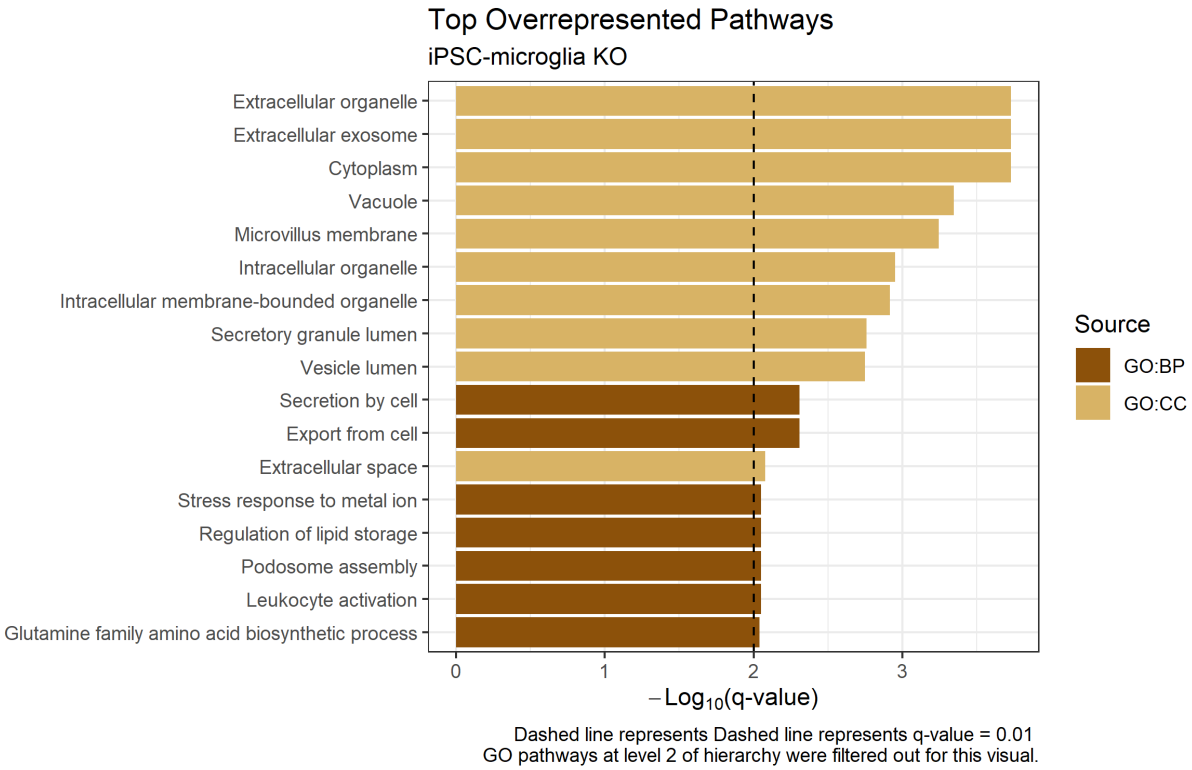

Table 1

Proteins significant in both MEFs and iPSC-microglia

		MEFs		iPSC-microglia	
Protein	Description	Log_2(KO)-Log_2(WT)	Adjusted P-value	Log_2(KO)-Log_2(WT)	Adjusted P-value
ALDH2	Aldehyde dehydrogenase 2, mitochondrial	1.04	3.16×10^{-3}	−23.04	2.46×10^{-13}
ARF5	ADP-ribosylation factor 5	1.15	3.51×10^{-2}	−1.27	6.12×10^{-3}
ASS1	Argininosuccinate synthetase 1	−2.68	1.58×10^{-5}	−1.03	2.41×10^{-2}
CDA	Cytidine deaminase	2.96	2.71×10^{-4}	−1.75	7.98×10^{-4}
CTNNA2	Catenin (cadherin associated protein), alpha 2	−1.05	2.81×10^{-2}	−22.96	6.29×10^{-15}
DNAAF5	Dynein, axonemal assembly factor 5	1.14	1.37×10^{-2}	−22.15	1.51×10^{-13}
FABP4	Fatty acid binding protein 4, adipocyte	27.75	1.06×10^{-7}	4.28	1.25×10^{-3}
FXN	Frataxin	1.43	4.50×10^{-2}	−24.79	7.11×10^{-11}
GLMP	Glycosylated lysosomal membrane protein	−1.10	6.45×10^{-3}	1.48	8.21×10^{-3}
HMGA2	High mobility group AT-hook 2	−3.63	2.86×10^{-3}	1.55	4.31×10^{-3}
IFIT3B	Interferon-induced protein with tetratricopeptide repeats 3B	−2.02	2.81×10^{-2}	−23.45	1.53×10^{-12}
KCMF1	Potassium channel modulatory factor 1	24.05	1.67×10^{-6}	−22.11	3.08×10^{-8}
LUZP1	Leucine zipper protein 1	24.86	2.31×10^{-7}	1.85	4.85×10^{-6}
MT1H	Metallothionein 1	1.24	1.24×10^{-2}	28.84	1.63×10^{-11}
MT1G	Metallothionein 1	1.24	1.24×10^{-2}	1.49	2.87×10^{-2}
PSMG4	Proteasome (prosome, macropain) assembly chaperone 4	1.52	2.10×10^{-2}	−22.57	2.30×10^{-13}
RPL22L1	Ribosomal protein L22 like 1	−1.12	3.14×10^{-2}	−23.47	2.05×10^{-14}
SCRN1	Secernin 1	1.13	3.46×10^{-3}	1.15	6.45×10^{-3}
SMC3	Structural maintenance of chromosomes 3	−1.30	2.57×10^{-5}	−22.71	5.42×10^{-12}
TRMT1	TRNA methyltransferase 1	−1.74	6.12×10^{-3}	−22.18	6.07×10^{-13}
TRNT1	TRNA nucleotidyl transferase, CCA-adding, 1	1.05	1.30×10^{-2}	−1.29	6.16×10^{-4}
TSPO	Translocator protein	3.00	5.00×10^{-3}	−1.13	2.94×10^{-2}
TUBAL3	Tubulin, alpha-like 3	−2.66	2.11×10^{-3}	−23.56	4.69×10^{-12}

Note: There is only one MT1 protein in MEFs while iPSC-microglia have two subtypes.
Cells are highlighted to indicate whether proteins were significant in: MEF WT, MEF KO, iPSC-microglia WT, iPSC-microglia KO

Table 2

Shared Significant Pathways

		Significance Values			
Term ID	Name	MEF WT	MEF KO	iPSC-microglia WT	iPSC-microglia KO
GO:BP					
GO:0033554	Cellular response to stress	4.46×10^{-3}	2.28×10^{-3}	3.59×10^{-4}	—
GO:0048519	Negative regulation of biological process	3.69×10^{-5}	4.60×10^{-3}	—	—
GO:1901565	Organonitrogen compound catabolic process	1.07×10^{-4}	9.55×10^{-7}	—	—
GO:1901564	Organonitrogen compound metabolic process	8.72×10^{-3}	1.83×10^{-6}	—	—
GO:CC					
GO:0005737	Cytoplasm	1.40×10^{-22}	7.06×10^{-33}	8.54×10^{-8}	1.86×10^{-4}
GO:0005829	Cytosol	3.61×10^{-20}	4.16×10^{-9}	7.26×10^{-14}	—
GO:0043231	Intracellular membrane-bounded organelle	1.01×10^{-8}	5.37×10^{-11}	1.25×10^{-7}	1.22×10^{-3}
GO:0043229	Intracellular organelle	5.91×10^{-10}	1.15×10^{-12}	1.04×10^{-7}	1.12×10^{-3}
GO:0031090	Organelle membrane	—	7.77×10^{-5}	3.21×10^{-3}	—
GO:0005773	Vacuole	—	—	3.37×10^{-3}	4.51×10^{-4}
GO:MF					
GO:1901265	Nucleoside phosphate binding	1.30×10^{-4}	1.34×10^{-3}	5.64×10^{-4}	—

Note: GO pathways at level 2 of hierarchy were filtered out for this table

Table 3

Proteins returning PubMed Fetch Results for Shared Pathways "Intracellular membrane-bounded organelle," "intracellular organelle," "organelle membrane," and "vacuole"

		MEFs		iPSC-microglia	
Protein	Description	Log_2(KO)-Log_2(WT)	Adjusted P-value	Log_2(KO)-Log_2(WT)	Adjusted P-value
AARS2	Alanyl-tRNA synthetase 2, mitochondrial	1.51	4.57×10^{-3}	—	—
AK1	Adenylate kinase 1	1.11	1.25×10^{-3}	0.67	6.96×10^{-2}
ANXA1	Annexin A1	−1.45	2.36×10^{-4}	−0.07	7.75×10^{-1}
APOC3	Apolipoprotein C3	—	—	24.49	1.09×10^{-13}
ASAH1	N-acylsphingosine amidohydrolase 1	−2.67	9.15×10^{-4}	0.42	4.93×10^{-2}
CALML5	Calmodulin like 5	—	—	1.09	3.02×10^{-2}
CD14	CD14 molecule	—	—	−3.48	8.61×10^{-6}
CD4	CD4 molecule	—	—	−23.46	4.50×10^{-13}
CD44	CD44 molecule (Indian blood group)	—	—	−0.42	4.56×10^{-2}
CDK5	Cyclin-dependent kinase 5	1.12	2.36×10^{-2}	−0.22	1.83×10^{-1}
CDK9	Cyclin-dependent kinase 9 (CDC2-related kinase)	1.01	2.86×10^{-3}	—	—
CHI3L1	Chitinase 3 like 1	—	—	−1.04	3.36×10^{-2}
CTSZ	Cathepsin Z	2.58	2.12×10^{-4}	0.22	4.06×10^{-1}
CYLD	CYLD lysine 63 deubiquitinase	23.97	7.23×10^{-8}	—	—
CYP27A1	Cytochrome P450 family 27 subfamily A member 1	—	—	−1.03	2.62×10^{-5}
DBT	Dihydrolipoamide branched chain transacylase E2	27.02	4.44×10^{-7}	0.46	3.19×10^{-1}
DES	Desmin	—	—	−25.79	2.98×10^{-12}
DNAJB6	DnaJ heat shock protein family (Hsp40) member B6	0.34	4.16×10^{-2}	23.85	1.09×10^{-13}
DUSP3	Dual specificity phosphatase 3 (vaccinia virus phosphatase VH1-related)	−1.05	6.41×10^{-3}	0.21	2.90×10^{-1}
DYSF	Dysferlin	28.08	1.71×10^{-7}	−0.07	9.15×10^{-1}
GLUL	Glutamate-ammonia ligase	—	—	1.53	8.80×10^{-3}
GNS	Glucosamine (N-acetyl)-6-sulfatase	−1.32	5.21×10^{-4}	0.50	3.06×10^{-2}
GPNMB	Glycoprotein (transmembrane) nmb	−29.25	2.13×10^{-7}	0.02	9.63×10^{-1}
HNRNPA2B1	Heterogeneous nuclear ribonucleoprotein A2/B1	24.15	7.83×10^{-6}	−0.43	2.17×10^{-1}
ITM2B	Integral membrane protein 2B	−1.34	1.20×10^{-1}	−21.41	3.09×10^{-12}
JUNB	Jun B proto-oncogene	25.06	1.58×10^{-5}	—	—
MAOA	Monoamine oxidase A	−1.28	2.10×10^{-3}	—	—
MT1	Metallothionein 1	1.24	1.24×10^{-2}	—	—
MT2	Metallothionein 2	3.16	1.64×10^{-3}	—	—
PCNA	Proliferating cell nuclear antigen	−1.06	4.57×10^{-4}	−0.46	2.97×10^{-1}
PLCG2	Phospholipase C, gamma 2	5.36	2.15×10^{-3}	−0.20	4.84×10^{-1}
PML	Promyelocytic leukemia	−1.74	1.43×10^{-2}	−0.50	2.45×10^{-1}
PTGS2	Prostaglandin-endoperoxide synthase 2	25.60	2.02×10^{-7}	—	—
ROCK2	Rho-associated coiled-coil containing protein kinase 2	−2.79	4.70×10^{-2}	0.02	9.73×10^{-1}
S100A6	S100 calcium binding protein A6 (calcyclin)	−0.40	2.41×10^{-2}	−1.94	2.26×10^{-3}
SNCA	Synuclein, alpha	−26.75	1.40×10^{-7}	0.72	5.12×10^{-3}
SRSF4	Serine and arginine rich splicing factor 4	—	—	−26.34	1.38×10^{-11}
TIA1	Cytotoxic granule-associated RNA binding protein 1	1.48	8.07×10^{-3}	1.91	1.96×10^{-2}
TPM3	Tropomyosin 3, gamma	−0.22	6.54×10^{-1}	24.53	2.35×10^{-15}
TRP53	Transformation related protein 53	29.11	5.15×10^{-9}	—	—
TSPO	Translocator protein	3.00	5.00×10^{-3}	−1.13	2.94×10^{-2}
UBE2E1	Ubiquitin conjugating enzyme E2 E1	—	—	−20.63	3.52×10^{-12}

PubMed fetch used queries Q_GRN2 and Q_FTD1.
Cells are highlighted to indicate whether proteins were significant in: MEF WT, MEF KO, iPSC-microglia WT, iPSC-microglia KO

Supplemental Figure 1

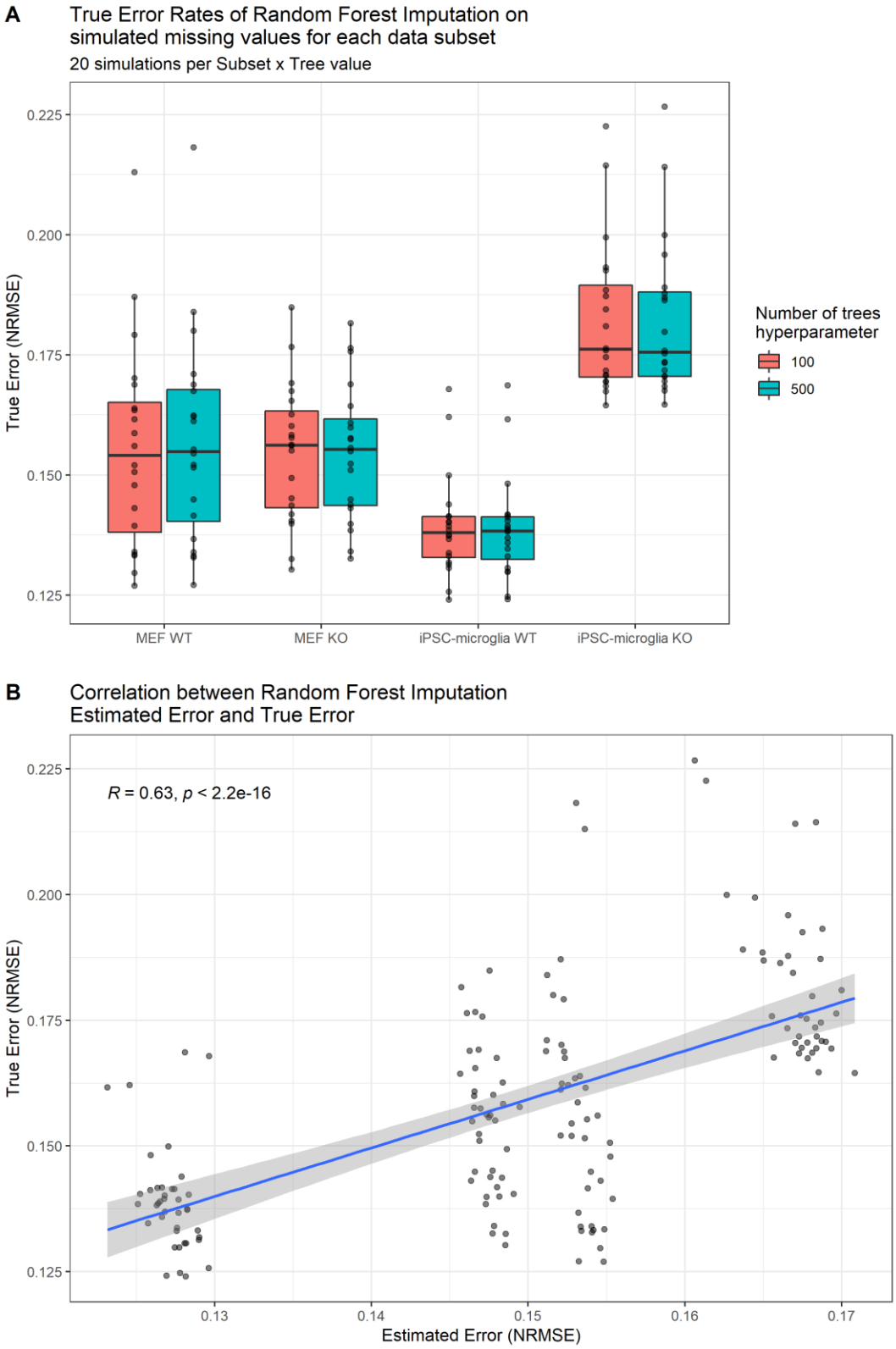

Supplemental Table 1

Shared Significant Pathways

		Significance Values			
Term ID	Name	MEF WT	MEF KO	iPSC-microglia WT	iPSC-microglia KO
GO:BP					
GO:0009058	Biosynthetic process	1.67×10^{-3}	5.99×10^{-3}	—	—
GO:0009056	Catabolic process	3.79×10^{-3}	7.04×10^{-10}	6.42×10^{-3}	—
GO:0071840	Cellular component organization or biogenesis	9.27×10^{-11}	—	3.20×10^{-3}	—
GO:0033554	Cellular response to stress	4.46×10^{-3}	2.28×10^{-3}	3.59×10^{-4}	—
GO:0072359	Circulatory system development	3.33×10^{-6}	4.69×10^{-3}	—	—
GO:0051179	Localization	1.64×10^{-3}	—	—	4.90×10^{-3}
GO:0033036	Macromolecule localization	5.46×10^{-3}	—	1.60×10^{-3}	—
GO:0008152	Metabolic process	2.80×10^{-4}	4.66×10^{-10}	—	—
GO:0048519	Negative regulation of biological process	3.69×10^{-5}	4.60×10^{-3}	—	—
GO:0055114	Obsolete oxidation-reduction process	9.60×10^{-3}	4.87×10^{-10}	—	—
GO:1901565	Organonitrogen compound catabolic process	1.07×10^{-4}	9.55×10^{-7}	—	—
GO:1901564	Organonitrogen compound metabolic process	8.72×10^{-3}	1.83×10^{-6}	—	—
GO:0065009	Regulation of molecular function	1.20×10^{-3}	1.30×10^{-4}	—	—
GO:0009628	Response to abiotic stimulus	4.85×10^{-3}	—	2.57×10^{-3}	—
GO:0006979	Response to oxidative stress	2.89×10^{-5}	4.62×10^{-5}	—	—
GO:0006950	Response to stress	2.66×10^{-7}	5.33×10^{-5}	3.68×10^{-3}	—
GO:0044281	Small molecule metabolic process	1.93×10^{-6}	8.87×10^{-16}	2.03×10^{-3}	—
GO:CC					
GO:0110165	Cellular anatomical entity	8.77×10^{-6}	1.10×10^{-3}	—	—
GO:0005737	Cytoplasm	1.40×10^{-22}	7.06×10^{-33}	8.54×10^{-8}	1.86×10^{-4}
GO:0005829	Cytosol	3.61×10^{-20}	4.16×10^{-9}	7.26×10^{-14}	—
GO:0012505	Endomembrane system	4.57×10^{-4}	—	1.03×10^{-3}	4.40×10^{-3}
GO:0005622	Intracellular anatomical structure	3.75×10^{-18}	8.20×10^{-21}	2.18×10^{-11}	9.96×10^{-4}
GO:0043231	Intracellular membrane-bounded organelle	1.01×10^{-8}	5.37×10^{-11}	1.25×10^{-7}	1.22×10^{-3}
GO:0043229	Intracellular organelle	5.91×10^{-10}	1.15×10^{-12}	1.04×10^{-7}	1.12×10^{-3}
GO:0005764	Lysosome	—	—	5.36×10^{-3}	1.86×10^{-4}
GO:0043227	Membrane-bounded organelle	3.09×10^{-7}	1.21×10^{-11}	2.71×10^{-6}	1.22×10^{-3}
GO:0043226	Organelle	5.83×10^{-9}	6.55×10^{-14}	1.98×10^{-7}	2.99×10^{-3}
GO:0031090	Organelle membrane	—	7.77×10^{-5}	3.21×10^{-3}	—
GO:0005773	Vacuole	—	—	3.37×10^{-3}	4.51×10^{-4}
GO:0031982	Vesicle	—	—	1.06×10^{-3}	9.96×10^{-4}
GO:MF					
GO:0043168	Anion binding	5.49×10^{-4}	1.19×10^{-6}	2.76×10^{-3}	—
GO:0005488	Binding	3.64×10^{-5}	1.92×10^{-3}	—	—
GO:0097367	Carbohydrate derivative binding	2.78×10^{-5}	—	4.16×10^{-3}	—
GO:0003824	Catalytic activity	3.48×10^{-5}	8.05×10^{-19}	2.09×10^{-3}	—
GO:0019899	Enzyme binding	4.45×10^{-4}	3.71×10^{-3}	—	—
GO:0016787	Hydrolase activity	—	8.53×10^{-4}	9.19×10^{-3}	—
GO:0042802	Identical protein binding	5.39×10^{-6}	1.32×10^{-6}	—	—
GO:0043167	Ion binding	1.86×10^{-3}	2.02×10^{-7}	—	—
GO:1901265	Nucleoside phosphate binding	1.30×10^{-4}	1.34×10^{-3}	5.64×10^{-4}	—
GO:0016491	Oxidoreductase activity	1.82×10^{-4}	7.73×10^{-10}	—	—
GO:0005515	Protein binding	1.01×10^{-10}	3.26×10^{-3}	—	—
GO:0036094	Small molecule binding	5.54×10^{-4}	1.82×10^{-6}	1.63×10^{-4}	—

1. Onyike, C.U., *The Epidemiology of Frontotemporal Dementia.* 2013. **25**(2): p. 130-7.
2. Cruts, M., S. Kumar-Singh, and C. Van Broeckhoven, *Progranulin mutations in ubiquitin-positive frontotemporal dementia linked to chromosome 17q21.* Curr Alzheimer Res, 2006. **3**(5): p. 485-91.
3. Gijselinck, I., et al., *Progranulin locus deletion in frontotemporal dementia.* Hum Mutat, 2008. **29**(1): p. 53-8.
4. Yu, C.E., et al., *The spectrum of mutations in progranulin: a collaborative study screening 545 cases of neurodegeneration.* Arch Neurol, 2010. **67**(2): p. 161-70.
5. Rademakers, R., M. Neumann, and I.R. Mackenzie, *Advances in understanding the molecular basis of frontotemporal dementia.* Nat Rev Neurol, 2012. **8**(8): p. 423-34.
6. Young, J.J., et al., *Frontotemporal dementia: latest evidence and clinical implications.* Ther Adv Psychopharmacol, 2018. **8**(1): p. 33-48.
7. Smith, K.R., et al., *Strikingly different clinicopathological phenotypes determined by progranulin-mutation dosage.* Am J Hum Genet, 2012. **90**(6): p. 1102-7.
8. Kamate, M., M. Detroja, and V. Hattiholi, *Neuronal ceroid lipofuscinosis type-11 in an adolescent.* Brain Dev, 2019. **41**(6): p. 542-545.
9. Palmer, D.N., et al., *Different patterns of hydrophobic protein storage in different forms of neuronal ceroid lipofuscinosis (NCL, Batten disease).* Neuropediatrics, 1997. **28**(1): p. 45-8.
10. Almeida, M.R., et al., *Portuguese family with the co-occurrence of frontotemporal lobar degeneration and neuronal ceroid lipofuscinosis phenotypes due to progranulin gene mutation.* Neurobiol Aging, 2016. **41**: p. 200.e1-200.e5.
11. Canafoglia, L., et al., *Recurrent generalized seizures, visual loss, and palinopsia as phenotypic features of neuronal ceroid lipofuscinosis due to progranulin gene mutation.* Epilepsia, 2014. **55**(6): p. e56-9.
12. Finch, N., et al., *Plasma progranulin levels predict progranulin mutation status in frontotemporal dementia patients and asymptomatic family members.* Brain, 2009. **132**(Pt 3): p. 583-91.
13. Bhandari, V., R.G. Palfree, and A. Bateman, *Isolation and sequence of the granulin precursor cDNA from human bone marrow reveals tandem cysteine-rich granulin domains.* Proc Natl Acad Sci U S A, 1992. **89**(5): p. 1715-9.
14. Plowman, G.D., et al., *The epithelin precursor encodes two proteins with opposing activities on epithelial cell growth.* J Biol Chem, 1992. **267**(18): p. 13073-8.
15. Shoyab, M., et al., *Epithelins 1 and 2: isolation and characterization of two cysteine-rich growth-modulating proteins.* Proc Natl Acad Sci U S A, 1990. **87**(20): p. 7912-6.
16. Zhang, Y., et al., *An RNA-sequencing transcriptome and splicing database of glia, neurons, and vascular cells of the cerebral cortex.* J Neurosci, 2014. **34**(36): p. 11929-47.
17. Gass, J., et al., *Progranulin regulates neuronal outgrowth independent of sortilin.* Mol Neurodegener, 2012. **7**: p. 33.
18. Van Damme, P., et al., *Progranulin functions as a neurotrophic factor to regulate neurite outgrowth and enhance neuronal survival.* J Cell Biol, 2008. **181**(1): p. 37-41.
19. Jian, J., J. Konopka, and C. Liu, *Insights into the role of progranulin in immunity, infection, and inflammation.* J Leukoc Biol, 2013. **93**(2): p. 199-208.
20. Hu, F., et al., *Sortilin-mediated endocytosis determines levels of the frontotemporal dementia protein, progranulin.* Neuron, 2010. **68**(4): p. 654-67.
21. Lee, W.C., et al., *Targeted manipulation of the sortilin-progranulin axis rescues progranulin haploinsufficiency.* Hum Mol Genet, 2014. **23**(6): p. 1467-78.
22. Holler, C.J., et al., *Intracellular Proteolysis of Progranulin Generates Stable, Lysosomal Granulins that Are Haploinsufficient in Patients with Frontotemporal Dementia Caused by GRN Mutations.* eNeuro, 2017. **4**(4).
23. Zhou, X., et al., *Prosaposin facilitates sortilin-independent lysosomal trafficking of progranulin.* J Cell Biol, 2015. **210**(6): p. 991-1002.

24. Beel, S., et al., *Progranulin functions as a cathepsin D chaperone to stimulate axonal outgrowth in vivo.* Hum Mol Genet, 2017. **26**(15): p. 2850-2863.
25. Butler, V.J., et al., *Progranulin Stimulates the in vitro Maturation of pro-Cathepsin D at Acidic pH.* J Mol Biol, 2019.
26. Butler, V.J., et al., *Multi-Granulin Domain Peptides Bind to Pro-Cathepsin D and Stimulate Its Enzymatic Activity More Effectively Than Progranulin in Vitro.* Biochemistry, 2019.
27. Valdez, C., et al., *Progranulin-mediated deficiency of cathepsin D results in FTD and NCL-like phenotypes in neurons derived from FTD patients.* Hum Mol Genet, 2017. **26**(24): p. 4861-4872.
28. Chen, Y., et al., *Progranulin associates with hexosaminidase A and ameliorates GM2 ganglioside accumulation and lysosomal storage in Tay-Sachs disease.* Journal of Molecular Medicine, 2018. **96**(12): p. 1359-1373.
29. Jian, J., et al., *Progranulin Recruits HSP70 to beta-Glucocerebrosidase and Is Therapeutic Against Gaucher Disease.* EBioMedicine, 2016. **13**: p. 212-224.
30. Jian, J., et al., *Association Between Progranulin and Gaucher Disease.* EBioMedicine, 2016. **11**: p. 127-137.
31. Zhou, X., T. Kukar, and R. Rademakers, *Lysosomal Dysfunction and Other Pathomechanisms in FTLD: Evidence from Progranulin Genetics and Biology.* Adv Exp Med Biol, 2021. **1281**: p. 219-242.
32. Kleinberger, G., et al., *Mechanisms of granulin deficiency: lessons from cellular and animal models.* Mol Neurobiol, 2013. **47**(1): p. 337-60.
33. Chang, M.C., et al., *Progranulin deficiency causes impairment of autophagy and TDP-43 accumulation.* J Exp Med, 2017. **214**(9): p. 2611-2628.
34. Gotzl, J.K., et al., *Common pathobiochemical hallmarks of progranulin-associated frontotemporal lobar degeneration and neuronal ceroid lipofuscinosis.* Acta Neuropathol, 2014. **127**(6): p. 845-60.
35. Tanaka, Y., et al., *Possible involvement of lysosomal dysfunction in pathological changes of the brain in aged progranulin-deficient mice.* Acta Neuropathol Commun, 2014. **2**: p. 78.
36. Ward, M.E., et al., *Individuals with progranulin haploinsufficiency exhibit features of neuronal ceroid lipofuscinosis.* Sci Transl Med, 2017. **9**(385).
37. Arrant, A.E., et al., *Progranulin Gene Therapy Improves Lysosomal Dysfunction and Microglial Pathology Associated with Frontotemporal Dementia and Neuronal Ceroid Lipofuscinosis.* J Neurosci, 2018. **38**(9): p. 2341-2358.
38. Gotzl, J.K., et al., *Early lysosomal maturation deficits in microglia triggers enhanced lysosomal activity in other brain cells of progranulin knockout mice.* Mol Neurodegener, 2018. **13**(1): p. 48.
39. Jian, J., A. Hettinghouse, and C.J. Liu, *Progranulin acts as a shared chaperone and regulates multiple lysosomal enzymes.* Genes Dis, 2017. **4**(3): p. 125-126.
40. Zhou, X., et al., *Regulation of cathepsin D activity by the FTLD protein progranulin.* Acta Neuropathol, 2017. **134**(1): p. 151-153.
41. Zhou, X., et al., *Progranulin deficiency leads to reduced glucocerebrosidase activity.* PLoS One, 2019. **14**(7): p. e0212382.
42. Evers, B.M., et al., *Lipidomic and Transcriptomic Basis of Lysosomal Dysfunction in Progranulin Deficiency.* Cell Rep, 2017. **20**(11): p. 2565-2574.
43. Kim, W.S., et al., *Lipidomics Analysis of Behavioral Variant Frontotemporal Dementia: A Scope for Biomarker Development.* Front Neurol, 2018. **9**: p. 104.
44. Lee, J.Y., O.C. Marian, and A.S. Don, *Defective Lysosomal Lipid Catabolism as a Common Pathogenic Mechanism for Dementia.* Neuromolecular Med, 2021. **23**(1): p. 1-24.
45. Marschallinger, J., et al., *Lipid-droplet-accumulating microglia represent a dysfunctional and proinflammatory state in the aging brain.* Nature Neuroscience, 2020. **23**(2): p. 194-208.
46. Stekhoven, D.J. and P. Bühlmann, *MissForest--non-parametric missing value imputation for mixed-type data.* Bioinformatics, 2012. **28**(1): p. 112-8.

47. Jin, L., et al., *A comparative study of evaluating missing value imputation methods in label-free proteomics.* Scientific Reports, 2021. **11**(1): p. 1760.
48. Oba, S., et al., *A Bayesian missing value estimation method for gene expression profile data.* Bioinformatics, 2003. **19**(16): p. 2088-2096.
49. Venneti, S., C.A. Wiley, and J. Kofler, *Imaging microglial activation during neuroinflammation and Alzheimer's disease.* J Neuroimmune Pharmacol, 2009. **4**(2): p. 227-43.
50. Zhang, J., *Mapping neuroinflammation in frontotemporal dementia with molecular PET imaging.* J Neuroinflammation, 2015. **12**: p. 108.
51. Götzl, J.K., et al., *Opposite microglial activation stages upon loss of PGRN or TREM2 result in reduced cerebral glucose metabolism.* EMBO Molecular Medicine, 2019. **11**(6): p. e9711.
52. Tanaka, Y., et al., *Exacerbated inflammatory responses related to activated microglia after traumatic brain injury in progranulin-deficient mice.* Neuroscience, 2013. **231**: p. 49-60.
53. Tanaka, Y., et al., *Increased lysosomal biogenesis in activated microglia and exacerbated neuronal damage after traumatic brain injury in progranulin-deficient mice.* Neuroscience, 2013. **250**: p. 8-19.
54. Lui, H., et al., *Progranulin Deficiency Promotes Circuit-Specific Synaptic Pruning by Microglia via Complement Activation.* Cell, 2016. **165**(4): p. 921-35.
55. Andrews, G.K., *Regulation of metallothionein gene expression.* Prog Food Nutr Sci, 1990. **14**(2-3): p. 193-258.
56. Zatta, P., et al., *Metallothionein-I-II and GFAP positivity in the brains from frontotemporal dementia patients.* J Alzheimers Dis, 2005. **8**(2): p. 109-16; discussion 209-15.
57. Kolberg, L., et al., *gprofiler2- an R package for gene list functional enrichment analysis and namespace conversion toolset g:Profiler.* F1000Research, 2020. **9 (ELIXIR)**(709).
58. *The Gene Ontology resource: enriching a GOld mine.* Nucleic Acids Res, 2021. **49**(D1): p. D325-d334.
59. Ashburner, M., et al., *Gene ontology: tool for the unification of biology. The Gene Ontology Consortium.* Nat Genet, 2000. **25**(1): p. 25-9.
60. Kanehisa, M. and S. Goto, *KEGG: kyoto encyclopedia of genes and genomes.* Nucleic Acids Res, 2000. **28**(1): p. 27-30.
61. Griss, J., et al., *ReactomeGSA - Efficient Multi-Omics Comparative Pathway Analysis.* Mol Cell Proteomics, 2020. **19**(12): p. 2115-2125.
62. Martens, M., et al., *WikiPathways: connecting communities.* Nucleic Acids Res, 2021. **49**(D1): p. D613-d621.
63. Supek, F., et al., *REVIGO Summarizes and Visualizes Long Lists of Gene Ontology Terms.* PLOS ONE, 2011. **6**(7): p. e21800.
64. Schlicker, A., et al., *A new measure for functional similarity of gene products based on Gene Ontology.* BMC Bioinformatics, 2006. **7**(1): p. 302.
65. Aggarwal, S. and A.K. Yadav, *False Discovery Rate Estimation in Proteomics*, in *Statistical Analysis in Proteomics*, K. Jung, Editor. 2016, Springer New York: New York, NY. p. 119-128.
66. Root, J., et al., *Lysosome dysfunction as a cause of neurodegenerative diseases: Lessons from frontotemporal dementia and amyotrophic lateral sclerosis.* Neurobiol Dis, 2021. **154**: p. 105360.
67. Huang, M., et al., *Network analysis of the progranulin-deficient mouse brain proteome reveals pathogenic mechanisms shared in human frontotemporal dementia caused by GRN mutations.* Acta Neuropathol Commun, 2020. **8**(1): p. 163.
68. Dobson-Stone, C., et al., *CYLD is a causative gene for frontotemporal dementia - amyotrophic lateral sclerosis.* Brain, 2020. **143**(3): p. 783-799.
69. Oyston, L.J., et al., *Rapid in vitro quantification of TDP-43 and FUS mislocalisation for screening of gene variants implicated in frontotemporal dementia and amyotrophic lateral sclerosis.* Sci Rep, 2021. **11**(1): p. 14881.
70. Eyo, U.B. and L.-J. Wu, *Microglia: Lifelong patrolling immune cells of the brain.* Progress in Neurobiology, 2019. **179**: p. 101614.

71. Tarassishin, L., et al., *Anti-viral and anti-inflammatory mechanisms of the innate immune transcription factor interferon regulatory factor 3: relevance to human CNS diseases.* J Neuroimmune Pharmacol, 2013. **8**(1): p. 132-44.
72. Ahmed, R.M., et al., *Systemic metabolism in frontotemporal dementia.* Neurology, 2014. **83**(20): p. 1812-8.
73. Kim, W.S., et al., *Altered High Density Lipoprotein Composition in Behavioral Variant Frontotemporal Dementia.* Front Neurosci, 2018. **12**: p. 847.
74. Sugama, S., et al., *Frontal lobe dementia with abnormal cholesterol metabolism and heterozygous mutation in sterol 27-hydroxylase gene (CYP27).* J Inherit Metab Dis, 2001. **24**(3): p. 379-92.
75. Kolter, T. and K. Sandhoff, *Lysosomal degradation of membrane lipids.* FEBS Lett, 2010. **584**(9): p. 1700-12.
76. Arrant, A.E., et al., *Impaired β-glucocerebrosidase activity and processing in frontotemporal dementia due to progranulin mutations.* Acta Neuropathol Commun, 2019. **7**(1): p. 218.
77. Valdez, C., et al., *Progranulin mutations result in impaired processing of prosaposin and reduced glucocerebrosidase activity.* Hum Mol Genet, 2020. **29**(5): p. 716-726.
78. Sapir, A., et al., *Controlled sumoylation of the mevalonate pathway enzyme HMGS-1 regulates metabolism during aging.* Proceedings of the National Academy of Sciences, 2014. **111**(37): p. E3880-E3889.
79. Go, G.W. and A. Mani, *Low-density lipoprotein receptor (LDLR) family orchestrates cholesterol homeostasis.* Yale J Biol Med, 2012. **85**(1): p. 19-28.
80. Ho, W.Y., et al., *TDP-43 mediates SREBF2-regulated gene expression required for oligodendrocyte myelination.* J Cell Biol, 2021. **220**(9).
81. Kleinberger, G., et al., *Increased caspase activation and decreased TDP-43 solubility in progranulin knockout cortical cultures.* Journal of Neurochemistry, 2010. **115**(3): p. 735-747.
82. Li, F. and H. Zhang, *Lysosomal Acid Lipase in Lipid Metabolism and Beyond.* Arterioscler Thromb Vasc Biol, 2019. **39**(5): p. 850-856.
83. Parveen, F., et al., *Role of Ceramidases in Sphingolipid Metabolism and Human Diseases.* Cells, 2019. **8**(12).
84. Lin, M.T. and M.F. Beal, *Mitochondrial dysfunction and oxidative stress in neurodegenerative diseases.* Nature, 2006. **443**(7113): p. 787-795.
85. Olszewska, D.A., et al., *Genetics of Frontotemporal Dementia.* Curr Neurol Neurosci Rep, 2016. **16**(12): p. 107.
86. Lines, G., et al., *Modelling frontotemporal dementia using patient-derived induced pluripotent stem cells.* Mol Cell Neurosci, 2020. **109**: p. 103553.
87. Gao, J., et al., *TDP-43 proteinopathy and mitochondrial abnormalities in neurodegeneration.* Mol Cell Neurosci, 2019. **100**: p. 103396.
88. Kreiter, N., et al., *Age-dependent neurodegeneration and organelle transport deficiencies in mutant TDP43 patient-derived neurons are independent of TDP43 aggregation.* Neurobiology of Disease, 2018. **115**: p. 167-181.
89. Danial, N.N. and S.J. Korsmeyer, *Cell Death: Critical Control Points.* Cell, 2004. **116**(2): p. 205-219.
90. Bui, M., et al., *Rab32 modulates apoptosis onset and mitochondria-associated membrane (MAM) properties.* J Biol Chem, 2010. **285**(41): p. 31590-602.
91. Mandrioli, J., et al., *ALS and FTD: Where RNA metabolism meets protein quality control.* Semin Cell Dev Biol, 2020. **99**: p. 183-192.
92. Taylor, J.P., R.H. Brown, and D.W. Cleveland, *Decoding ALS: from genes to mechanism.* Nature, 2016. **539**(7628): p. 197-206.
93. Klaips, C.L., G.G. Jayaraj, and F.U. Hartl, *Pathways of cellular proteostasis in aging and disease.* Journal of Cell Biology, 2018. **217**(1): p. 51-63.

94. Lilienbaum, A., *Relationship between the proteasomal system and autophagy.* Int J Biochem Mol Biol, 2013. **4**(1): p. 1-26.
95. Serpente, M., et al., *Profiling of ubiquitination pathway genes in peripheral cells from patients with frontotemporal dementia due to C9ORF72 and GRN mutations.* Int J Mol Sci, 2015. **16**(1): p. 1385-94.
96. De Conti, L., et al., *TDP-43 affects splicing profiles and isoform production of genes involved in the apoptotic and mitotic cellular pathways.* Nucleic acids research, 2015. **43**(18): p. 8990-9005.
97. Polymenidou, M., et al., *Long pre-mRNA depletion and RNA missplicing contribute to neuronal vulnerability from loss of TDP-43.* Nature neuroscience, 2011. **14**(4): p. 459-468.
98. Chou, C.C., et al., *TDP-43 pathology disrupts nuclear pore complexes and nucleocytoplasmic transport in ALS/FTD.* Nat Neurosci, 2018. **21**(2): p. 228-239.
99. Woerner, A.C., et al., *Cytoplasmic protein aggregates interfere with nucleocytoplasmic transport of protein and RNA.* Science, 2016. **351**(6269): p. 173-176.
100. Protter, D.S. and R. Parker, *Principles and properties of stress granules.* Trends in cell biology, 2016. **26**(9): p. 668-679.
101. Jain, S., et al., *ATPase-modulated stress granules contain a diverse proteome and substructure.* Cell, 2016. **164**(3): p. 487-498.
102. Alami, N.H., et al., *Axonal transport of TDP-43 mRNA granules is impaired by ALS-causing mutations.* Neuron, 2014. **81**(3): p. 536-543.
103. Ghosh, S. and R.L. Geahlen, *Stress Granules Modulate SYK to Cause Microglial Cell Dysfunction in Alzheimer's Disease.* EBioMedicine, 2015. **2**(11): p. 1785-98.
104. Guo, M., et al., *Microglial Exosomes in Neurodegenerative Disease.* Front Mol Neurosci, 2021. **14**: p. 630808.
105. Trotta, T., et al., *Microglia-derived extracellular vesicles in Alzheimer's Disease: A double-edged sword.* Biochem Pharmacol, 2018. **148**: p. 184-192.
106. Gleason, A.M., et al., *The Role of Exosomes in Lysosomal Storage Disorders.* Biomolecules, 2021. **11**(4).
107. Zhang, J., et al., *Neurotoxic microglia promote TDP-43 proteinopathy in progranulin deficiency.* Nature, 2020. **588**(7838): p. 459-465.
108. Brites, D. and A. Fernandes, *Neuroinflammation and Depression: Microglia Activation, Extracellular Microvesicles and microRNA Dysregulation.* Front Cell Neurosci, 2015. **9**: p. 476.
109. Zhou, X., et al., *Impaired prosaposin lysosomal trafficking in frontotemporal lobar degeneration due to progranulin mutations.* 2017. **8**.
110. Misasi, R., et al., *Biochemistry and neurobiology of prosaposin: a potential therapeutic neuro-effector.* Cent Nerv Syst Agents Med Chem, 2009. **9**(2): p. 119-31.
111. Sandhoff, R. and K. Sandhoff, *Emerging concepts of ganglioside metabolism.* FEBS Lett, 2018. **592**(23): p. 3835-3864.
112. Nita, D.A., S.E. Mole, and B.A. Minassian, *Neuronal ceroid lipofuscinoses.* Epileptic Disord, 2016. **18**(S2): p. 73-88.
113. Singh, R., et al., *Autophagy regulates lipid metabolism.* Nature, 2009. **458**(7242): p. 1131-5.
114. Jaishy, B. and E.D. Abel, *Lipids, lysosomes, and autophagy.* J Lipid Res, 2016. **57**(9): p. 1619-35.
115. Jana, B.A., et al., *Cytosolic lipid excess-induced mitochondrial dysfunction is the cause or effect of high fat diet-induced skeletal muscle insulin resistance: a molecular insight.* Mol Biol Rep, 2019. **46**(1): p. 957-963.
116. Lawrence, R.E. and R. Zoncu, *The lysosome as a cellular centre for signalling, metabolism and quality control.* Nat Cell Biol, 2019. **21**(2): p. 133-142.
117. Schlaepfer, I.R. and M. Joshi, *CPT1A-mediated Fat Oxidation, Mechanisms, and Therapeutic Potential.* Endocrinology, 2020. **161**(2).
118. Strauss, K., et al., *Exosome Secretion Ameliorates Lysosomal Storage of Cholesterol in Niemann-Pick Type C Disease **. Journal of Biological Chemistry, 2010. **285**(34): p. 26279-26288.

119. Yvan-Charvet, L., et al., *Combined deficiency of ABCA1 and ABCG1 promotes foam cell accumulation and accelerates atherosclerosis in mice.* The Journal of Clinical Investigation, 2007. **117**(12): p. 3900-3908.
120. Yvan-Charvet, L., et al., *Increased inflammatory gene expression in ABC transporter-deficient macrophages: free cholesterol accumulation, increased signaling via toll-like receptors, and neutrophil infiltration of atherosclerotic lesions.* Circulation, 2008. **118**(18): p. 1837-47.
121. Tanaka, Y., et al., *Progranulin regulates lysosomal function and biogenesis through acidification of lysosomes.* Hum Mol Genet, 2017. **26**(5): p. 969-988.
122. Khatri, P., M. Sirota, and A.J. Butte, *Ten years of pathway analysis: current approaches and outstanding challenges.* PLoS Comput Biol, 2012. **8**(2): p. e1002375.
123. Markmann, S., et al., *Quantitative Proteome Analysis of Mouse Liver Lysosomes Provides Evidence for Mannose 6-phosphate-independent Targeting Mechanisms of Acid Hydrolases in Mucolipidosis II.* Mol Cell Proteomics, 2017. **16**(3): p. 438-450.
124. Ponnaiyan, S., et al., *Comprehensive draft of the mouse embryonic fibroblast lysosomal proteome by mass spectrometry based proteomics.* Sci Data, 2020. **7**(1): p. 68.
125. Seyfried, N.T., et al., *A Multi-network Approach Identifies Protein-Specific Co-expression in Asymptomatic and Symptomatic Alzheimer's Disease.* Cell Syst, 2017. **4**(1): p. 60-72.e4.
126. Fantini, D., *easyPubMed: Search and Retrieve Scientific Publication Recrods from PubMed*. 2019: https://www.data-pulse.com/dev_site/easypubmed/.